Monthly Notices
of the
ROYAL ASTRONOMICAL SOCIETY

MNRAS **476,** 5216–5232 (2018)
Advance Access publication 2018 February 27

doi:10.1093/mnras/sty525

The GALAH survey: properties of the Galactic disc(s) in the solar neighbourhood

L. Duong,[1⋆] K. C. Freeman,[1⋆] M. Asplund,[1⋆] L. Casagrande,[1] S. Buder,[2] K. Lind,[2,3] M. Ness,[2] J. Bland-Hawthorn,[4] G. M. De Silva,[4,5] V. D'Orazi,[6] J. Kos,[4] G. F. Lewis,[4] J. Lin,[1] S. L. Martell,[7] K. Schlesinger,[1] S. Sharma,[4] J. D. Simpson,[5] D. B. Zucker,[8] T. Zwitter,[9] B. Anguiano,[8,10] G. S. Da Costa,[1] E. Hyde,[11] J. Horner,[12] P. R. Kafle,[13] D. M. Nataf,[1,14] W. Reid,[15,16] D. Stello,[4,8,17] Y.-S. Ting[1,18,19,20] and R. F. G. Wyse[14]

[1]*Research School of Astronomy and Astrophysics, Australian National University, ACT 2611, Australia*
[2]*Max-Planck-Institute for Astronomy, Koenigstuhl 17, D-69117 Heidelberg, Germany*
[3]*Department of Physics and Astronomy, Uppsala University, Box 516, SE-751 20 Uppsala, Sweden*
[4]*Sydney Institute for Astronomy, School of Physics A28, University of Sydney, NSW 2006, Australia*
[5]*Australian Astronomical Observatory, North Ryde, NSW 1670, Australia*
[6]*INAF – Osservatorio Astronomico di Padova, Vicolo dell'Osservatorio 5, I-35122 Padova, Italy*
[7]*School of Physics, University of New South Wales, NSW 2052, Australia*
[8]*Department of Physics and Astronomy, Macquarie University, NSW 2109, Australia*
[9]*Faculty of Mathematics and Physics, University of Ljubljana, Jadranska 19, 1000 Ljubljana, Slovenia*
[10]*Department of Astronomy, University of Virginia, PO Box 400325 Charlottesville, VA 22904-4325, USA*
[11]*Western Sydney University, Locked Bag 1797, Penrith South DC, NSW 1797, Australia*
[12]*University of Southern Queensland, Toowoomba, Queensland 4350, Australia*
[13]*ICRAR, The University of Western Australia, 35 Stirling Highway, Crawley, WA 6009, Australia*
[14]*Center for Astrophysical Sciences and Department of Physics and Astronomy, The Johns Hopkins University, Baltimore, MD 21218, USA*
[15]*Department of Physics and Astronomy, Macquarie University, Sydney, NSW 2109, Australia*
[16]*Western Sydney University, Locked bag 1797, Penrith South DC, NSW 2751, Australia*
[17]*Department of Physics and Astronomy, Stellar Astrophysics Centre, Aarhus University, DK-8000 Aarhus C, Denmark*
[18]*Institute for Advanced Study, Princeton NJ 08540, USA*
[19]*Department of Astrophysical Sciences, Princeton University, Princeton NJ 08544, USA*
[20]*Observatories of the Carnegie Institution of Washington, Pasadena CA 91101, USA*

Accepted 2018 February 22. Received 2018 February 21; in original form 2017 December 8

ABSTRACT

Using data from the GALAH pilot survey, we determine properties of the Galactic thin and thick discs near the solar neighbourhood. The data cover a small range of Galactocentric radius ($7.9 \lesssim R_{\rm GC} \lesssim 9.5$ kpc), but extend up to 4 kpc in height from the Galactic plane, and several kpc in the direction of Galactic anti-rotation (at longitude $260^\circ \leq \ell \leq 280^\circ$). This allows us to reliably measure the vertical density and abundance profiles of the chemically and kinematically defined 'thick' and 'thin' discs of the Galaxy. The thin disc (low-α population) exhibits a steep negative vertical metallicity gradient, at $\mathrm{d[M/H]/d}z = -0.18 \pm 0.01$ dex kpc^{-1}, which is broadly consistent with previous studies. In contrast, its vertical α-abundance profile is almost flat, with a gradient of $\mathrm{d}[\alpha/\mathrm{M}]/\mathrm{d}z = 0.008 \pm 0.002$ dex kpc^{-1}. The steep vertical metallicity gradient of the low-α population is in agreement with models where radial migration has a major role in the evolution of the thin disc. The thick disc (high-α population) has a weaker vertical metallicity gradient $\mathrm{d[M/H]/d}z = -0.058 \pm 0.003$ dex kpc^{-1}. The α-abundance of the thick disc is nearly constant with height, $\mathrm{d}[\alpha/\mathrm{M}]/\mathrm{d}z = 0.007 \pm 0.002$ dex kpc^{-1}. The negative gradient in metallicity and the small gradient in [α/M] indicate that the high-α population experienced a settling phase, but also formed prior to the onset of major Type Ia supernova enrichment. We explore the implications of the distinct α-enrichments and narrow [α/M] range of the sub-populations in the context of thick disc formation.

Key words: surveys – stars: abundances – Galaxy: disc – Galaxy: evolution – Galaxy: formation.

⋆ E-mail: ly.duong@anu.edu.au (LD); kenneth.freeman@anu.edu.au (KCF); martin.asplund@anu.edu.au (MA)

1 INTRODUCTION

The Milky Way is believed to have a thick disc, similar to those observed photometrically in external disc galaxies (Burstein 1979; Tsikoudi 1979; Dalcanton & Bernstein 2002; Yoachim & Dalcanton 2006; Comerón et al. 2015). The ubiquity of thick discs indicates that they are an integral part of disc galaxy evolution. The Galactic thick disc was originally discussed as a distinct structural component by Gilmore & Reid (1983),[1] who showed that the vertical stellar density profile at the Galactic South pole was best described by two exponentials. Much debate has since ensued over the origin and properties of the Galactic thick disc. Most notably some authors have argued that it may not be a discrete component (Norris 1987; Nemec & Nemec 1993; Schönrich & Binney 2009; Bovy, Rix & Hogg 2012a).

The chemical properties of the local thick disc have been well characterized by multiple spectroscopic studies. The consensus is that it is older (e.g. Wyse & Gilmore 1988; Haywood et al. 2013; Bensby, Feltzing & Oey 2014), kinematically hotter (Chiba & Beers 2000), and more metal-poor and α-rich than the thin disc (Prochaska et al. 2000; Fuhrmann 2008; Bensby et al. 2014; Furhmann et al. 2016). The enhanced α-abundances indicate that thick disc stars were enriched by Type Ia supernovae (SNe II) over a short period of time, before SNe Ia contribution of iron-peak elements took effect in earnest. The thick disc is thought to have formed within $\approx$1–3 Gyr (Gratton et al. 2000; Mashonkina et al. 2003), although Haywood et al. (2013) suggested a slightly longer formation time-scale of 4–5 Gyr.

At the solar annulus, many authors have observed a gap between thin and thick disc stars in the α-abundance ([α/M]) versus metallicity ([M/H]) plane. This is widely interpreted as evidence that the thick disc is a distinct component. In recent literature, the 'thick disc' is often defined chemically as the α-enhanced population. Large-scale abundance maps from the APOGEE survey show that two distinct sequences in [α/M] versus [M/H] are observed at all galactocentric radii, although the fractions of stars in the two sequences vary greatly with position in the Galaxy. In the inner Galaxy ($3 < R_{\rm GC} < 5$ kpc), and at large heights above the Galactic plane, the high-α sequence dominates. Beyond galactocentric radius $R_{\rm GC} \approx 9$ kpc, its density decreases significantly (Hayden et al. 2015). This observation is in line with the short scalelength of about 2 kpc for the chemical thick disc (Bensby et al. 2011; Cheng et al. 2012; Bovy et al. 2012b, 2016). The concentration of the older, α-enhanced population to the inner disc also indicates that the thick disc formed inside-out (Matteucci & François 1989; Burkert, Truran & Hensler 1992; Samland & Gerhard 2003; Bird et al. 2013). In contrast to the chemically defined thick disc of the Milky Way, the photometrically defined thick discs of external galaxies are more extended, with scalelengths comparable to thin disc scalelengths (e.g. Yoachim & Dalcanton 2006; Ibata, Mouhcine & Rejkuba 2009). Similarly, selecting Milky Way thick disc stars using non-chemical criteria leads to a thick disc with scalelength longer than that of the thin disc (e.g. Ojha 2001).

While its scalelength is fairly well constrained, the scaleheight of the thick disc is still contentious (see Bland-Hawthorn & Gerhard 2016, and references therein). Gilmore & Reid (1983) estimated the thick disc exponential scaleheight to be 1.35 kpc from star counts, similar to measurements made by photometric decomposition of Milky Way analogues (e.g. Ibata et al. 2009). More recent estimates find the thick disc scaleheight to be significantly shorter, and there is still some scatter in the measurements (Jurić et al. 2008; Kordopatis et al. 2011; Bovy et al. 2012b, 2016). Furthermore, results from high-resolution spectroscopic surveys have raised doubts on the existence of a structurally distinct thick disc, even if there are clearly two populations with distinct α-enhancements. Bovy et al. (2016) finds a smooth transition in scaleheights for mono-abundance populations (MAPs), as does Mackereth et al. (2017) for mono-age populations, where more α-enhanced and older stars populate increasingly greater heights. Martig et al. (2016b) also showed that, due to flaring of the disc (Rahimi, Carrell & Kawata 2014; Minchev et al. 2015; Kawata et al. 2017), the geometrically thick part of the disc has a large age dispersion, whereas the chemical 'thick disc' (high-α population) has a narrow age range. This may also explain why the chemically defined thick disc of the Milky Way has a short scalelength, while surface brightness measurements of geometrical thick discs in external galaxies indicate that they are radially much more extended.

Several theoretical models have been proposed for thick disc formation and explain its observed properties. Thick discs may arise from external heating processes such as dwarf satellite accretion (Abadi et al. 2003) or minor merger events (Quinn & Goodman 1986; Quinn, Hernquist & Fullagar 1993; Kazantzidis et al. 2008; Villalobos & Helmi 2008). The fast internal evolution of gravitationally unstable clumpy discs at a high redshift (Bournaud, Elmegreen & Martig 2009; Forbes, Krumholz & Burkert 2012) or gas-rich mergers at a high red-shift (Brook et al. 2004, 2005) could form a thick disc. The turbulent interstellar medium observed in disc galaxies at high redshift may also be associated with thick disc formation (e.g. Wisnioski et al. 2015). Radial migration of stars (Sellwood & Binney 2002), where stars are transported outwards and gain vertical height to form a thick disc, is another possibility that has been extensively discussed (Schönrich & Binney 2009; Minchev & Famaey 2010; Loebman et al. 2011; Roškar et al. 2012; Schönrich & McMillan 2017). Although there is evidence for radial migration in the thin disc, such as the presence of very metal-rich low-α stars in the solar neighbourhood (Haywood 2008; Casagrande et al. 2011) and the skewness of metallicity distribution functions (MDFs) at different Galactic radii (Hayden et al. 2015; Loebman et al. 2016), the role of radial migration in thick disc formation is still unclear, and is not supported by some observed properties of the thick disc (high-α) population (e.g. Haywood et al. 2013; Recio-Blanco et al. 2014; Bovy et al. 2016). Vera-Ciro et al. (2014) showed in their simulation that radial migration can have strong effects on the thin disc, but not the thick disc. Aumer, Binney & Schönrich (2016) found that in their standard model, outwardly migrating stars are not responsible for the creation of the thick disc, but thick discs can form in models with high baryon fractions. However, in their high-baryon models, the bar is too long, the young stars are too hot, and the disc is strongly flared.

Observational evidence to discern thick disc formation scenarios is still inconclusive. Earlier results, such as the lack of thick disc vertical metallicity gradient observed by Gilmore, Wyse & Jones (1995) and orbital eccentricity distributions by Sales et al. (2009) and Dierickx et al. (2010), favoured merger scenarios. More recent studies, most of which separate thin and thick disc stars by their metallicity or kinematics, indicate that the thick disc does have a vertical metallicity gradient (Chen et al. 2011; Katz et al. 2011; Kordopatis et al. 2011; Ruchti et al. 2011), but the gradients measured by these studies vary greatly due to their different methods of isolating the thick disc. Few studies report on the vertical abundance profile of the disc, although an accurate measurement of the

[1] See also Yoshii (1982).

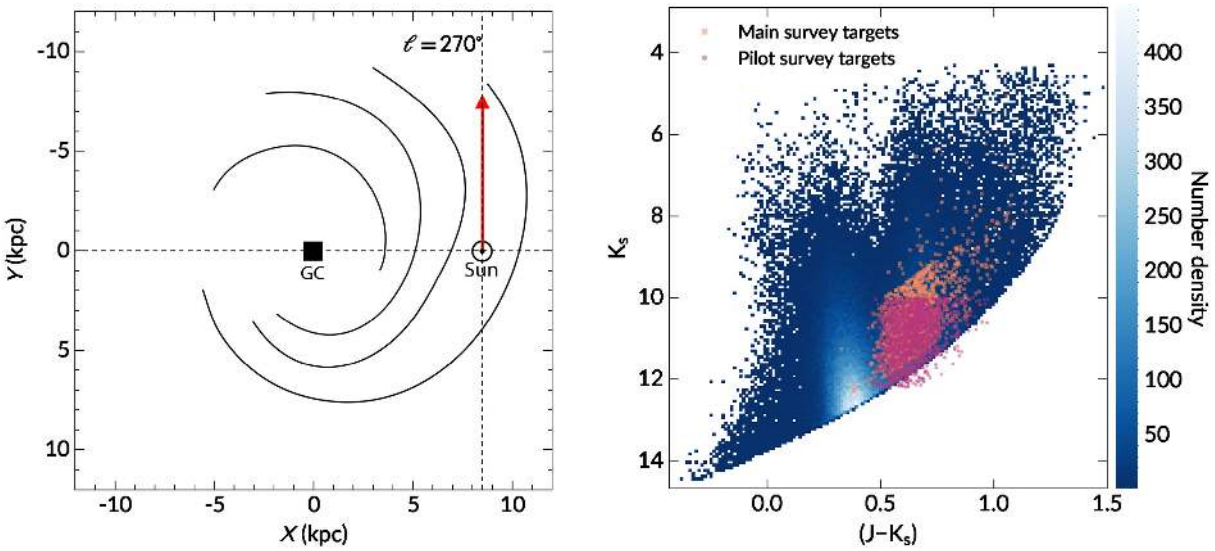

Figure 1. The location of observed fields and colour–magnitude selection of the GALAH main and pilot survey targets. Left-hand panel: a schematic view of the Milky Way, illustrating the targeted line of sight. We observe along $\ell \approx 270^\circ$ and at five latitudes below the plane. The spiral arms are shown as traced by H II gas, from Drimmel & Spergel (2001). Right-hand panel: The colour–magnitude selection of the stars in this analysis is shown against all GALAH input catalogue targets within the observed region (including special bright targets). The pilot survey has a simple magnitude cut, at bright and faint limits of $K_s = 10$ and 12, respectively. The main GALAH survey magnitude selection $12 < V_{JK} < 14$ appears as a stripe in the $(J - K_s)$ versus K_s plane. The pilot survey extends slightly fainter than the main survey, and the handful of stars falling outside of the main survey selection are from a bright field.

metallicity and abundance profile as a function of distance from the Galactic plane can provide important constraints for the evolution history of the disc.

This work is motivated by the current uncertainty about the formation and properties of the Galactic thick disc. The thick disc is important because its formation is a seemingly ubiquitous feature of disc galaxy evolution; its rapid formation and old population mean that it provides a detailed snap-shot of the conditions in the early Galaxy. Understanding how the thick disc formed and evolved will be central to chemical tagging efforts of current and future high-resolution massive spectroscopic surveys such as 4MOST (de Jong et al. 2011), *Gaia*-ESO (Gilmore et al. 2012), APOGEE (Majewski et al. 2017), GALAH[2] (De Silva et al. 2015), and WEAVE (Dalton et al. 2016).

We have used data from the first GALAH survey internal release to study the properties of the Galactic thick disc. We show that at the solar circle, the thick disc exhibits a non-negligible vertical metallicity gradient, and the thin disc shows a steep vertical metallicity gradient. We find that the mean α-element abundance does not vary significantly with height in either of the chemically and kinematically defined thick and thin discs.

The paper is structured as follows: Section 2 describes the stellar sample used in the analysis, including field and colour selection. Section 3 explains the methods of obtaining stellar parameters, abundances, and the distances, as well as how thin and thick disc components were defined. Section 4 explores the possible effects of our selection and how they were corrected for. Section 5 presents the results of metallicity, and the α-abundance variation with vertical height is described in Section 6. We discuss the implications of our results for the formation and evolution of the thick disc in Section 7, and summarize the work in Section 8.

[2] www.galah-survey.org

2 SAMPLE SELECTION

We present in this paper results from the GALAH survey internal data release v1.3. The data acquisition and reduction are described in Martell et al. (2017) and Kos et al. (2017), respectively. The stellar parameter and abundance determination are summarized in Section 3.1. Briefly, GALAH spectra cover four optical bands, at wavelengths located within the Johnson–Cousins *B*, *V*, *R*, *I* passbands, with resolving power $\lambda/\Delta\lambda \approx 28000$ (De Silva et al. 2015). The GALAH main-survey selects stars according to a simple magnitude criterion: $12 < V_{JK} < 14$, where the V_{JK} magnitude is estimated from 2MASS (Skrutskie et al. 2006) *J*, K_s photometry via the transformation

$$V_{JK} = K_s + 2(J - K_s + 0.14) + 0.382\,e^{(J-K_s-0.2)/0.50}. \quad (1)$$

The above equation is discussed further in Sharma et al. (2018, see their fig. 1). The magnitude selection in V_{JK} manifests as a $(J - K_s)$ colour dependence when plotted as function of other magnitudes, as shown in Fig. 1, right-hand panel.

In addition to normal survey fields, which follow the V_{JK} magnitude limit described above, GALAH also observed special fields, such as pilot survey fields (which included benchmark stars and clusters), and bright stars selected from the *Tycho*-2 catalogue (Martell et al. 2017), most of which also appear in the *Gaia* DR1 catalogue (Brown et al. 2016).

As part of the GALAH pilot survey, we conducted a study of the chemical properties and distribution of the Galactic thin and thick discs. Fields were chosen towards Galactic longitude $\ell = 270^\circ$, as shown in Fig. 1, left-hand panel. This longitude was chosen to maximize the asymmetric drift component between thin and thick disc stars (Gilmore, Wyse & Norris 2002; Wyse et al. 2006), thus making it easier to distinguish them by their kinematics. We observed fields at five latitudes: $b = -16^\circ, -22^\circ, -28^\circ, -34^\circ$, and -42°. Fig. 2 shows the distribution of observed stars in Galactic coordinates R_{GC} and $|z|$ (distances are derived as per Section 3.2). Adopting $R_{GC,\odot} = 8$ kpc, most of the stars are concentrated around

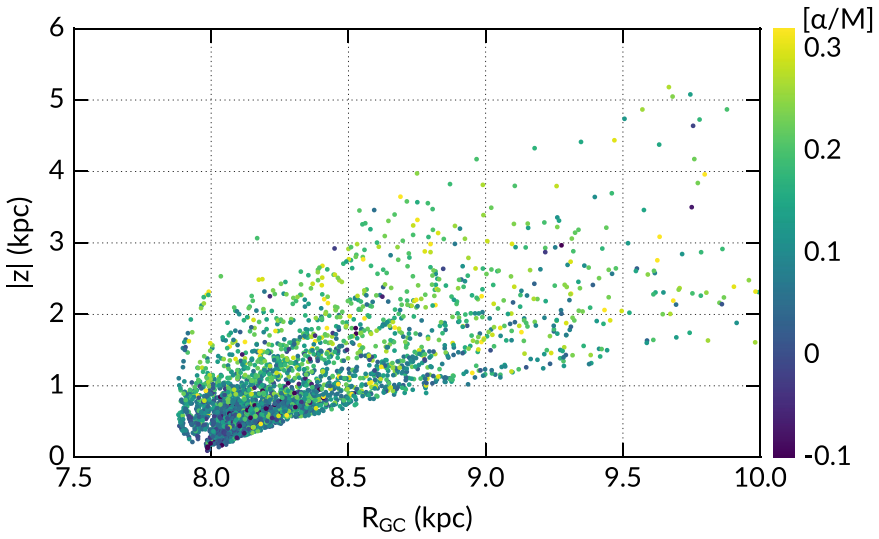

Figure 2. The distribution in Galactocentric radius and height below the plane for the entire sample, adopting $R_{GC,\odot} = 8$ kpc. There are a few stars (not shown) outside the limits $|z| > 6$ kpc and $R > 10$ kpc. Stars are colour-coded by α-abundances: Low-α stars lie typically closer to the plane, whereas α-enhanced stars are found at greater distances from the plane.

the solar radius, between $R_{GC} = 8$ and 8.5 kpc, and up to about 4 kpc in height below the Galactic plane. Since our longitude range is between $\ell = (260, 280)$, we also observed stars with $R_{GC} < 8$ kpc.

We chose to use only giants in this study to include a larger range of distances and heights from the plane. The magnitude limits of the main GALAH survey result in giants making up only about 25 per cent of stars observed. In order to increase the fraction of giants, a colour cut at $(J - K_s) > 0.45$ was imposed for the pilot survey prior to observations, which excludes turn-off stars and some dwarfs. We also extended the faint V_{JK}-magnitude limit of the pilot survey to 14.5 in order to observe a larger fraction of clump giants. Also included in this analysis are giants from the GALAH main-survey that fall within the same Galactic longitude–latitude range described above. The colour and magnitude selection for all stars included in the analysis is shown in Fig. 1.

3 DATA ANALYSIS

3.1 Stellar parameters and α abundances

The GALAH stellar parameters and abundances pipeline will be described in detail elsewhere; here, we seek to give a brief summary. The pipeline is a two-step process, involving spectral synthesis using SME (Spectroscopy Made Easy) (Valenti & Piskunov 1996; Piskunov & Valenti 2017) and the data-driven generative modelling approach of The Cannon (Ness et al. 2015). We identify a sample of stars with high signal-to-noise ratio (S/N), each visually inspected to be free of irregularities like unexpected continuum variations and large cosmic ray residuals. This set of stars serves as the training set, the labels of which are propagated to all other survey stars. The training set includes *Gaia* benchmark standards (Jofré et al. 2014; Heiter et al. 2015), whose parameters have been determined by non-spectroscopic methods; globular and open clusters and stars with accurate asteroseismic surface gravity from *K2* Campaign 1 (Stello et al. 2017). In total, there are ≈2500 training stars.

In the first step, stellar parameters for the training set are obtained with SME. Here, we use the MARCS model atmospheres (Gustafsson et al. 2008), and non-LTE corrections for Fe (Lind, Bergemann & Asplund 2012). SME syntheses of Hα and Hβ, and neutral and ionized lines of Ti, Sc, and Fe are used to determine T_{eff}, log g, [M/H],[3] v_{mic} (micro turbulence), and $V \sin i$ (rotational velocity), converging at the global minimum χ^2. The stellar parameters are fixed when individual abundances are computed for the α-elements Mg, Si, and Ti. The weighted average of these elements gives [α/M], and all abundances are scaled according to the Solar chemical composition of Grevesse, Asplund & Sauval (2007).

Although the GALAH wavelength range includes lines of the α-elements Ca and O, they are currently omitted from the weighted average because the Ca lines fall within problematic spectral regions (due to bad CCD pixels and/or sub-optimal data reduction), and the O I triplet at 7772–7775 Å is subjected to large non-LTE effects (Amarsi et al. 2015, 2016), which are not yet accounted for in the GALAH analysis pipeline. Relative to *Gaia* benchmark standards, SME produces accurate results with offsets in log g and [M/H] of −0.15 and −0.1 dex, respectively, in the sense that it underestimates these values. The same surface gravity offset is also observed when SME results are compared to asteroseismic log g obtained with oscillations from Stello et al. (2017). The offsets are constant across the Hertzsprung–Russell (HR) diagram, and are corrected by simply adding 0.15 and 0.1 dex to all log g and [M/H] values of the training set prior to parameter propagation with The Cannon (Sharma et al. 2018).

In the second step, The Cannon learns the training set parameters and abundances (*labels*) from SME, and builds a quadratic model at each pixel of the normalized spectrum[4] as a function of the labels (Ness et al. 2015). This model is then used to determine stellar parameters and abundances for all other survey spectra. In addition to the six primary labels described above, The Cannon uses a seventh

[3] We use [M/H] to denote metallicity to differentiate it from the actual iron abundance [Fe/H]. The metallicity reported in this data release is the iron abundance of the best-fitting atmospheric model and mostly measured from Fe lines. However, [M/H] values are close to the true iron abundances, and GALAH results presented elsewhere have used [Fe/H] to denote metallicity, which is equivalent to the [M/H] used here.

[4] The normalization method is described in Kos et al. (2017).

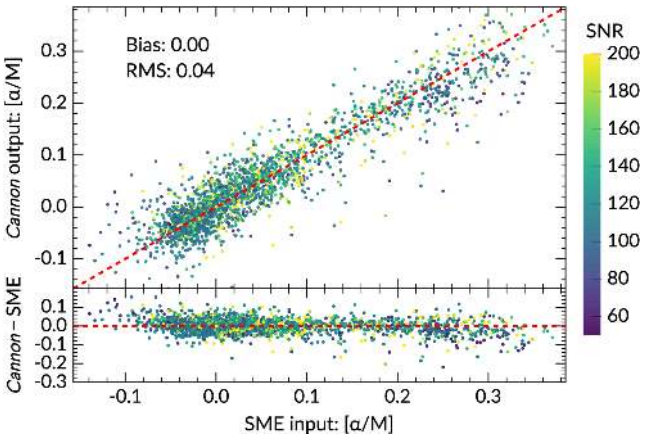

Figure 3. Cross-validation of The Cannon-output against SME input for the label [α/M]. Stars are colour coded by S/N in the 'green' arm of HERMES, the wavelength of which lies within the Johnson–Cousins *V*-band. The top panel shows the 1:1 relation between SME input and The Cannon-output. The bottom panel shows the distribution of the difference. The Cannon reproduces the SME input without bias, and to 0.04 dex precision.

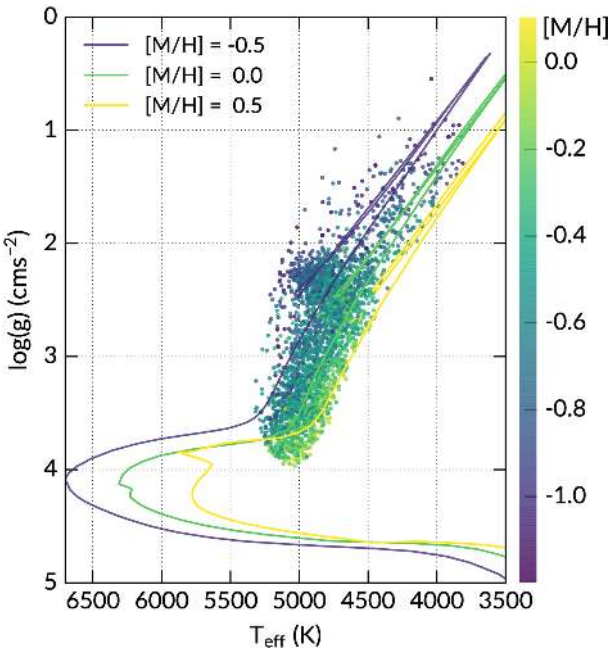

Figure 4. The *Kiel* diagram from The Cannon for the sample of stars in this analysis, colour coded by [M/H]. Over plotted are 4 Gyr PARSEC isochrones at metallicities indicated in the figure legend. The stellar parameters behave as predicted by the evolutionary tracks after bias corrections to The Cannon training set (see text for details).

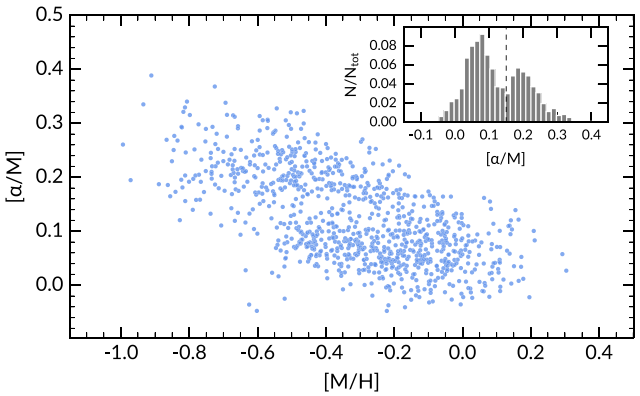

Figure 5. α-abundances as a function of metallicity for a sub-sample with S/N $\geq$ 80 per resolution element. There are two distinct abundance sequences corresponding to the thin disc (low-α) and the thick disc (high-α). Inset: histogram of the [α/M] distribution, the dotted line indicates [α/M] = 0.15, where the two populations appear to separate.

label, extinction $A(K_s)$, to minimize the effect of reddening and diffuse interstellar bands on [α/M] determination. The extinction for each star of the training set was estimated with the RJCE method (Majewski, Zasowski & Nidever 2011). We used 2MASS *H*-band and *WISE* 4.5-μm photometry (Wright et al. 2010), following procedures outlined in Zasowski et al. (2013). Parameter errors are estimated by cross-validating the input (SME) and output labels (The Cannon) for the training set. Cross-validation was done by partitioning the reference set into unique sub-samples, each consisting 20 per cent of the full set. Five tests were performed, each time a 20 per cent sub-sample is left out of the training step, and used only to validate the results. Fig. 3 shows the combined cross-validation outcomes of all five tests for label [α/M]. The training set results have also been successfully applied to the TESS-HERMES survey, and the error estimation of stellar labels except for [α/M] is shown in fig. 5 of Sharma et al. (2018). Overall, The Cannon achieves internal precisions of 47 K in T_{eff}, 0.13 dex in log *g*, 0.05 dex in [M/H], and 0.04 dex in [α/M], which are typical of the errors reported in this data release.

Fig. 4 shows The Cannon-derived stellar parameters for the full sample of giants selected for analysis. We have excluded most subgiants, turn-off and main-sequence stars. The Cannon is able to reproduce the accuracy and precision of SME such that all parameters follow the PARSEC isochrone tracks (Marigo et al. 2017) without further calibrations. The [α/M]–[M/H] plot is shown in Fig. 5 for a sub-sample of stars with S/N $\geq$ 80 per resolution element. We observe the two distinct α-tracks in the [α/M]–[M/H] plane: a low-α track extending from [M/H] $\approx$ 0.4 to $-$0.6, usually defined as the chemical thin disc, and a high-α track extending from [M/H] $\approx -$ 0.2 to $-$1, usually defined as the chemical thick disc. The typical precision of the [α/M] measurements is 0.04 dex, similar to that of [M/H].

We do not include stars with [M/H] ≤ -1 dex here, because few metal-poor stars could be used in the training set (the stars are rare, and typically have low S/N), rendering The Cannon results for metal-poor stars significantly less accurate. The Cannon has limited ability to extrapolate, which is evident in the comparison to *Gaia* benchmarks: stars with [M/H] < -1 have larger deviations from reference values (Sharma et al. 2018). This does, however, exclude the metal-weak thick disc from our analysis. We find that other studies that include the metal-poor extension of the thick disc, such as Katz et al. (2011); Ruchti et al. (2011) reported similar results to ours (see detailed discussion in Sections 5.2.2 and 6). Furthermore, there are few stars with [M/H] ≤ -1 dex to begin with (2 per cent of the full sample), so their exclusion may have small effects on the vertical gradients derived in later sections, but it is unlikely that this would have a major impact on our conclusions.

3.2 Distance determination

Distances are typically determined by isochrone fitting methods using the fundamental stellar parameters T_{eff}, log *g* and [M/H], and photometry. Theoretical constraints, such as stellar evolution and

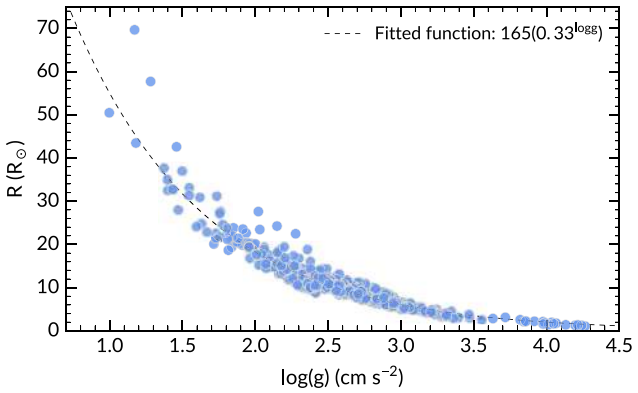

Figure 6. The correlation between stellar surface gravity and radius, data from the *Kepler* sample of Casagrande et al. (2014). The stellar radius as a function of log g is best described by an exponential.

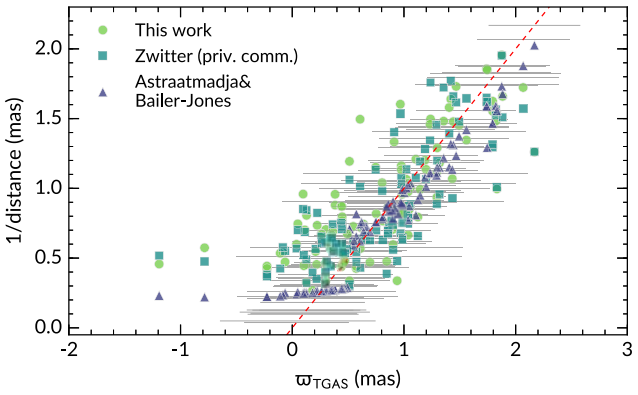

Figure 7. Comparison of distances derived from GALAH stellar parameters (this work/Zwitter) and Bayesian TGAS distances (Astraatmadja & Bailer-Jones). On the x-axis are TGAS parallaxes, and the grey horizontal bars indicate reported uncertainties (including systematic errors). There is a break in the Astraatmadja & Bailer-Jones (2016) values because a different prior is used for $\varpi < 0.5$ mas, which according to the authors is more accurate for large distances (see text for details). The y-axis shows inferred parallaxes from the three distance methods. The dashed line is the 1:1 correlation. As the parallax decreases, TGAS fractional errors become very large, and in some cases negative parallaxes are reported. Compared to TGAS, distances derived from GALAH stellar parameters have an overall scatter of ≈0.37 mas, which is within the typical TGAS uncertainty of 0.3 mas. For $\varpi < 0.5$ mas, there is a systematic offset between TGAS and IRFM/Zwitter distances of ≈0.3 mas.

initial mass functions (IMFs) have been included by Zwitter et al. (2010) and Burnett & Binney (2010), respectively, to obtain more accurate distances for the RAVE survey (Steinmetz et al. 2006). Isochrone distances are dependent on all fundamental parameters, but a strong dependence on [M/H] can cause correlated errors when trying to assess the metallicity distribution as a function of distance from the Galactic Centre or above the plane (Schlesinger et al. 2014; Anguiano et al. 2015). In this section, we describe an empirical method of distance determination that does not have such a strong dependence on inferred [M/H], which may be advantageous for our measurements of metallicity vertical gradients in Section 5.

To determine the distance, we exploit the relationship between stellar surface gravity and radius R using *Kepler* asteroseismic data from Casagrande et al. (2014). Fig. 6 shows the log g–R correlation and the exponential function that best fits the data. Using spectroscopically determined log g, we compute for each GALAH star a radius (in solar radii) using the function:

$$R_* = 165(0.33^{\log g}). \tag{2}$$

Note that starting from the definition of $g = GM/R_*^2$, where G is the gravitational constant, and M the mass of the star, we arrive at the formula:

$$R_*/\mathrm{R}_\odot = 10^{0.5(\log g_\odot - \log g)}, \tag{3}$$

which is equivalent to $165.59 * 0.316^{\log g}$, assuming that $M = \mathrm{M}_\odot$ and the solar log g is 4.438 068 cm s^{-2}. However, the function used to fit the data in Fig. 6 returns the minimum reduced-χ^2 (perhaps due to differences in the stellar mass compared to the assumed solar value), and is used instead.[5]

The absolute luminosity is estimated using the effective temperature and radius relation:

$$L = 4\pi R_*^2 \sigma T_{\rm eff}^4. \tag{4}$$

Finally, we interpolate the stellar parameters $T_{\rm eff}$, log g, [M/H] over a grid of synthetic spectra to determine the correction that needs to be applied to 2MASS J, H, $K_{\rm s}$ photometry to derive the bolometric flux $\mathcal{F}_{\rm bol}$.[6] We correct for extinction using the Schlegel, Finkbeiner & Davis (1998) map to de-redden the observed 2MASS magnitudes. This is done using extinction coefficients computed on-the-fly for the set of stellar parameters adopted (Casagrande et al. 2010). The distance is then simply

$$D = \left(\frac{L}{4\pi\mathcal{F}_{\rm bol}}\right)^{1/2}. \tag{5}$$

As is evident from Fig. 6, the log g–stellar radius relation is poorly constrained for log $g \leq 1.5$, because we have few seismic data points in this region and the scatter is larger. There are however relatively few stars with log $g < 1.5$ in our sample (see Fig. 4).

3.2.1 *Distance error estimate*

We tested the accuracy and precision of our distance determination method by comparing our results to the first *Gaia* data release (Brown et al. 2016, TGAS), which provides accurate parallaxes (ϖ) for bright stars in the *Tycho*-2 catalogue (Michalik, Lindegren & Hobbs 2015). Because of the brighter magnitude limit of *Tycho*-2, we only have a small overlap of about 100 stars for comparison. We also compare our distances to those of Astraatmadja & Bailer-Jones (2016), who computed Bayesian distances using TGAS parallaxes and Milky Way density models. Finally, we include a comparison between our method and that of Zwitter et al. (2010), which computes the distance modulus by fitting stellar parameters to their most likely isochrone counterparts.

Fig. 7 compares the unaltered TGAS parallaxes with the inferred parallaxes from the three distance methods. Distances from Astraatmadja & Bailer-Jones (2016) are median values of the posterior from their Milky Way density model. However, they note that the Milky Way model underestimates distances for $\varpi < 0.5$ mas when compared to Cepheid distances, as the model assumes that a star is more likely to be in the disc and photometric information is not used. Thus, the distances used here for $\varpi < 0.5$ are the median

[5] The typical difference between distances derived using $165.59 * 0.316^{\log g}$ and equation (3) is 13 per cent, which is comparable to the distance uncertainties (Section 3.2.1).

[6] Although [M/H] is used, the dependence of $\mathcal{F}_{\rm bol}$ on this parameter is minimal (Casagrande et al. 2010).

of the posterior from their exponentially decreasing density model with scalelength $L = 1.35$ kpc (Astraatmadja & Bailer-Jones 2016).

The comparison shows no systematic discrepancy for $\varpi_{\rm TGAS} > 0.5$ mas. The distances computed from our IRFM and the Zwitter et al. (2010) isochrone fitting method using the same spectroscopic parameters agree to within ≈15 per cent. Compared to TGAS, both the IRFM and isochrone fitting method have a standard deviation of 0.3 mas, which is well within the typical errors quoted for TGAS parallaxes. We noticed that the Bayesian distances from Astraatmadja & Bailer-Jones (2016) are slightly overestimated compared to TGAS between $\varpi_{\rm TGAS} = 1$ and 2 mas.

We do find an offset between all distance methods and the TGAS parallaxes for $\varpi_{\rm TGAS} = 0$–0.5 mas, where the TGAS values may be underestimated. For stars with $\varpi_{\rm TGAS} > 0$, the offset is 0.33 mas for the spectroscopic distances. Stassun & Torres (2016) found a similar offset, between TGAS and inferred parallaxes derived from eclipsing binaries; however, their results are applicable only to smaller distances, which is not seen in our results (see also Huber et al. 2017). A likely reason for the GALAH-TGAS offset is that TGAS uncertainties become very large at $\varpi < 0.5$ mas, so for a magnitude-limited sample, TGAS systematically scatters to smaller values.

In summary, we find that our distances are accurate compared to TGAS parallaxes and the Bayesian distances of Astraatmadja & Bailer-Jones (2016), albeit with an offset for $\varpi_{\rm TGAS} < 0.5$ mas. Overall, the standard deviation between the two spectroscopic methods is 17 per cent. Since both our method and the isochrone fitting method used the same set of stellar parameters, the comparison between them is indicative of their intrinsic uncertainties. Assuming that both methods contribute equally to the overall scatter, the internal uncertainty of each method is 12 per cent. This is the value we adopted as the our distance errors.

3.3 Separating the thin and thick disc populations

High-resolution spectroscopic studies show that the α-enhancement of local disc stars follows two distinct tracks (e.g. Adibekyan et al. 2011; Bensby et al. 2014). The high-α population is typically associated with the thick disc and has high velocity dispersion; the low-α stars are associated with the thin disc, with low velocity dispersion. The thick disc also has a larger rotational lag compared to the thin disc.

The thick disc can also be defined geometrically by star counts (Jurić et al. 2008; Chen et al. 2011), or by metallicity and kinematics (Katz et al. 2011; Kordopatis et al. 2011). The thin and thick discs do overlap in their spatial, metallicity, and kinematical distributions. Because of the two distinct sequences in [α/M]–[Fe/H] space, definition of the thick disc by its enhanced α-abundances relative to thin disc stars of the same metallicity is currently widely used (Adibekyan et al. 2013; Bensby et al. 2014; Haywood et al. 2015). However, the adopted dividing line between the high and low-α populations differs from author to author. Furthermore, some stars with thick disc chemistry have thin disc kinematics, and there are stars that lie in the intermediate region between the two [α/M] sequences. The 'thick disc' population that we are interested in is the stellar fossil of the turbulent epoch of fast star formation at high-z. Following this definition, we want to exclude the flaring outer thin disc, which contributes to the geometrical thick disc, and metal-rich stars that may have migrated from the inner thin disc.

To this end, we chose to separate the two components by fitting a mixture of Gaussian distributions using the Expectation-Minimization algorithm (Dempster, Laird & Rubin 1977). We use three variables: [M/H] and [α/M] and the radial velocity (RV), which, to the best of our knowledge, has not been done previously. At $\ell = 270^\circ$, the component of the rotational lag between the thin and thick disc along the line-of-sight is maximized for most of our fields, such that RV is a good proxy for V velocity (see also Kordopatis et al. 2017). Instead of using the Cartesian V space velocity component, which has significant proper motion errors, we use the precise GALAH RV to help separate the two populations (98 per cent of our survey stars have RV uncertainty <0.6 kms^{-1} according to Martell et al. 2017).

The PYTHON `scikit-learn` (Pedregosa et al. 2011) module `GaussianMixture` was used to perform the fitting. We assume that the data cube can be described by two multivariate Gaussians, each characterized by its three means and 3×3 covariance matrix: $\theta_j = (\mu_j, \Sigma_j)$, where $j = \{1, 2\}$, to represent the low- and high-α sequences. Note that Rojas-Arriagada et al. (2016) argue the [α/M] versus[M/H] distribution could be described by five components, but here we are not concerned with finding sub-components of the two α-sequences.

Given a set of data $(x_1, x_2, \ldots, x_n)$, the likelihood function is defined as

$$\mathcal{L}(\theta; x) = \prod_{i=1}^{n} \sum_{j=1}^{2} w_j f(x_i; \mu_j, \Sigma_j), \tag{6}$$

where f is the probability density function of a multivariate normal distribution and w_j is the weight of each distribution. The algorithm initializes with random guesses for $\theta = (w_j, \mu_j, \Sigma_j)$ and iterates until the log-likelihood is at minimum. The probability that a data point x_i belongs to component j is given by

$$P_j(x_i \mid \theta) = \frac{w_j f(x_i; \mu_j, \Sigma_j)}{w_1 f(x_i; \mu_1, \Sigma_1) + w_2 f(x_i, \mu_2, \Sigma_2)}, \tag{7}$$

where

$$P_1(x_i) + P_2(x_i) = 1. \tag{8}$$

Fig. 8 shows projections in the [α/M]–[M/H] and the RV–[α/M] planes, where two Gaussian components centred at [α/M] = 0.05 and [α/M] = 0.2 can be seen, each with a distinctive median RV. Stars are colour-coded by their thick disc probability. As expected, the high-α stars have much higher thick disc probability than the low-α stars. It is also apparent that stars with [M/H] between −0.4 and 0 are likely to be designated thin disc membership, because their radial velocities and metallicity more closely resemble that of thin disc stars. This is perhaps the most important distinction between our 'thick disc' definition and that of other studies: that the overall more α-enhanced population does not include the high metallicity, high-α population. This places important constraints on subsequent analyses and the interpretation of our results with respect to models of disc formation, as here we are assuming that the thick disc is almost exclusively old by excluding more metal-rich stars.

Furthermore, Fig. 8 indicates that there are 'transition stars', which have higher [α/M] than thin disc stars at the same metallicity and kinematics that lie between the two discs, making it is difficult to assign them to either population. We therefore assigned thin disc membership only to stars that have thick disc probability ≤0.1, which have [α/M] ≤ 0.15, consistent with the location of the 'gap' between high- and low- α populations for our data set. The majority of stars with thick disc probability between 0.1 and 0.5 have [α/M] values between 0.15 and 0.3 dex. These 'transition' stars are omitted from the analysis to minimize contamination in each defined population. Approximately 13 per cent of the overall sample are in the 'transition' category.

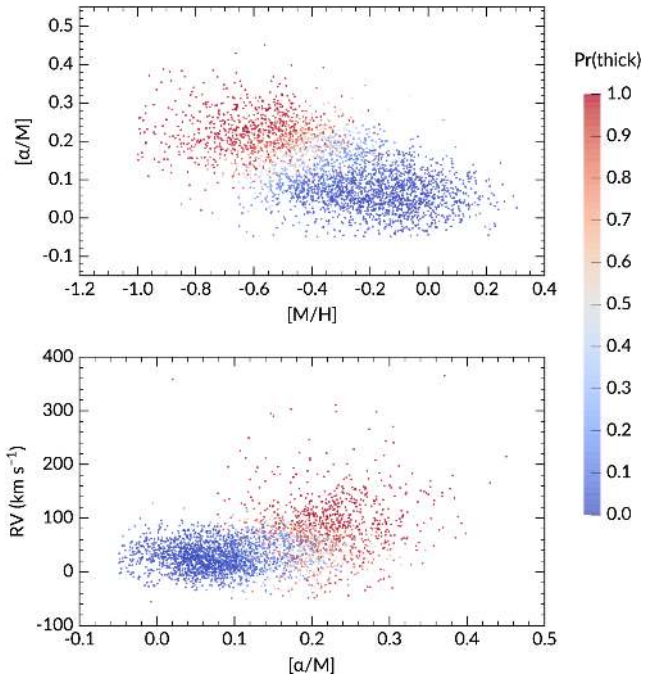

Figure 8. Results of the Gaussian mixture decomposition. Top panel: projection along the [α/M]–[M/H] plane. Bottom panel: projection along the [α/M]–RV plane, both colour-coded by the probability of a star belong to the thick disc. We can see that there are two well-defined populations in both projections; however, there are also plenty of stars that are difficult to place in either population. These stars have chemistry and kinematics that could belong to either of the classically defined 'thin' and 'thick' disc. Stars that are typically defined as thin disc by chemistry have Pr(thick) $\leq$ 0.1. Stars with typical thick disc chemistry however have a higher velocity dispersion and therefore a larger spread in probability, ranging from 0.6 $\leq$ Pr(thick) <1.

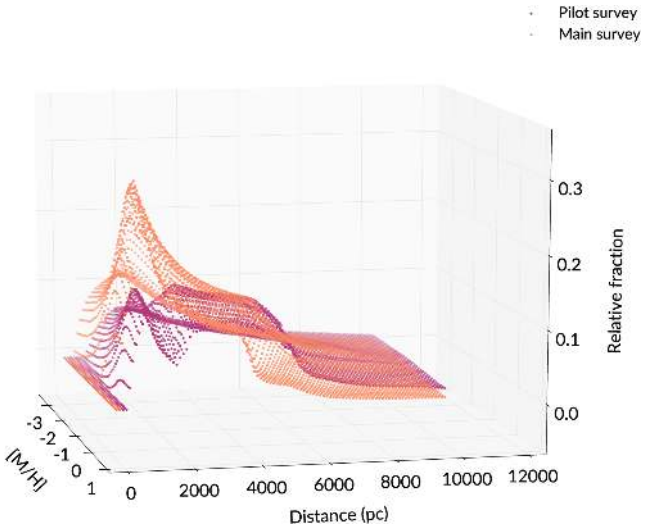

Figure 9. The relative probability of observing a particular star in the metallicity–distance plane given the colour–magnitude selection of GALAH pilot and main surveys. While we show the metallicity distribution up to [M/H] = −3 dex, we do not have any stars with [M/H] < −1 in our sample. The distance distribution is most affected by the colour–magnitude selection of the two surveys, with the pilot survey favouring more distant stars. The metallicity of both surveys peaks around solar, but compared to the main survey, the pilot survey has a larger fraction of stars that are more metal-poor.

4 SELECTION BIAS

Fig. 1, right-hand panel, shows that the pilot survey has a simple magnitude cut, $10 < K_s < 12$, while the main survey colour–magnitude selection appears to be a stripe in the $(J - K_s)_0$ versus K_s plane, from the criterion that $12 < V_{JK} < 14$. The main survey also observed some bright stars that fall outside the lower magnitude limit. In addition, the pilot survey purposely observed a larger fraction of stars at higher latitudes, which means that the population at low latitudes is underrepresented. These selection biases affect the resulting metallicity, distance (and therefore vertical height) distributions of the observed population. In this section, we aim to correct for these effects so that the underlying Galactic population can be correctly recovered.

4.1 Correcting for selection effects

4.1.1 Field selection bias

The first selection effect that we corrected was the bias from targeting particular fields. We purposely observed a larger relative fraction of stars at higher latitudes to target the thick disc, and thus biased against low-latitude stars.

To correct for this, we determined for each field the number of stars present in the observed sample compared with the number of photometric targets available for that field in the GALAH input catalogue, within the same magnitude limit, for example:

$$w_{\rm field} = \frac{N_{\rm observed}\ (12 < V_{JK} < 14)}{N_{\rm targets}\ (12 < V_{JK} < 14)}.$$

We dealt with the magnitude ranges of the pilot and main surveys separately. The limits used are $12 < V_{JK} < 14$ for main survey fields; $12 < V_{JK} < 14.5$ for pilot fields, and $9 < V_{JK} < 12$ for the bright field.

4.1.2 Magnitude and colour selection bias

Following Casagrande et al. (2016), we assessed the magnitude and colour selection bias by creating a synthetic population using BaSTI isochrones (Pietrinferni et al. 2004). From a data cube that spans 0.5–10 Gyr in age, −3–0.5 dex in metallicity and 10–10 000 pc in distance, each point in the age and metallicity plane is populated on the isochrones according to the Salpeter (1955) IMFs, with the distances providing apparent magnitudes for each population. We then applied the same apparent colour and magnitude cut as shown in Fig. 1 to obtain the ratio of stars observed with our selection function compared to the total number of stars that populate a given point in the age, metallicity, and distance cube. As in the previous section, the pilot and main survey selection functions are taken into account separately. Because there is no age information available for this sample, we integrated the observed probabilities over all ages for each point in the distance–metallicity plane. This implicitly assumes that the age distribution is flat in the solar neighbourhood (e.g. Edvardsson et al. 1993; Ting, Conroy & Goodman 2015). With this method, the effects of different evolutionary time-scales of each stellar population on the HR diagram are also taken into account via the IMFs.

Fig. 9 shows the relative fraction of stars observed after the colour–magnitude selection is applied. The most metal-poor and metal-rich stars are slightly biased against, similarly so for both the

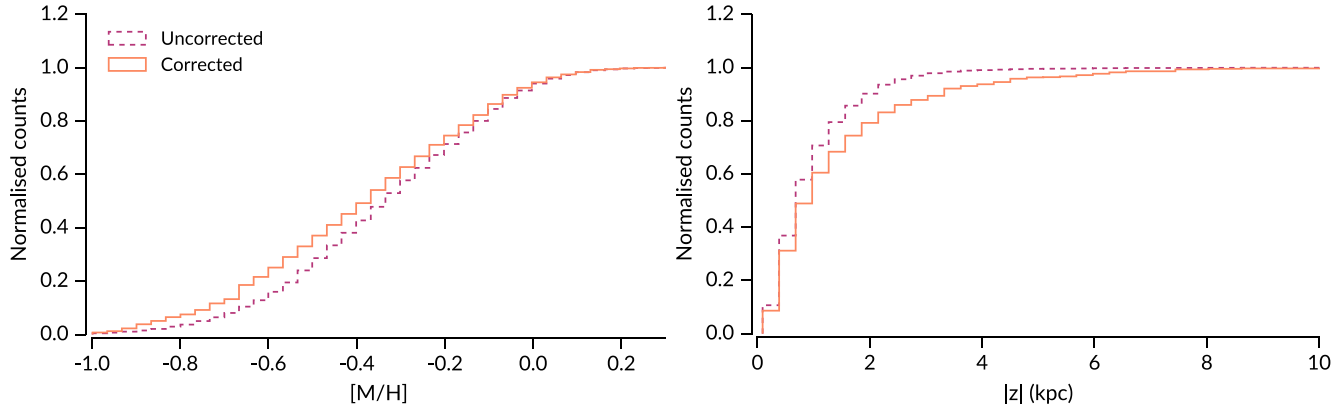

Figure 10. Cumulative histograms showing bias-uncorrected and corrected metallicity and height $|z|$ distributions. Left-hand panel: [M/H] distribution. Right-hand panel: height distribution. Typically the corrections account for the bias against stars that are more metal-poor and further from the plane.

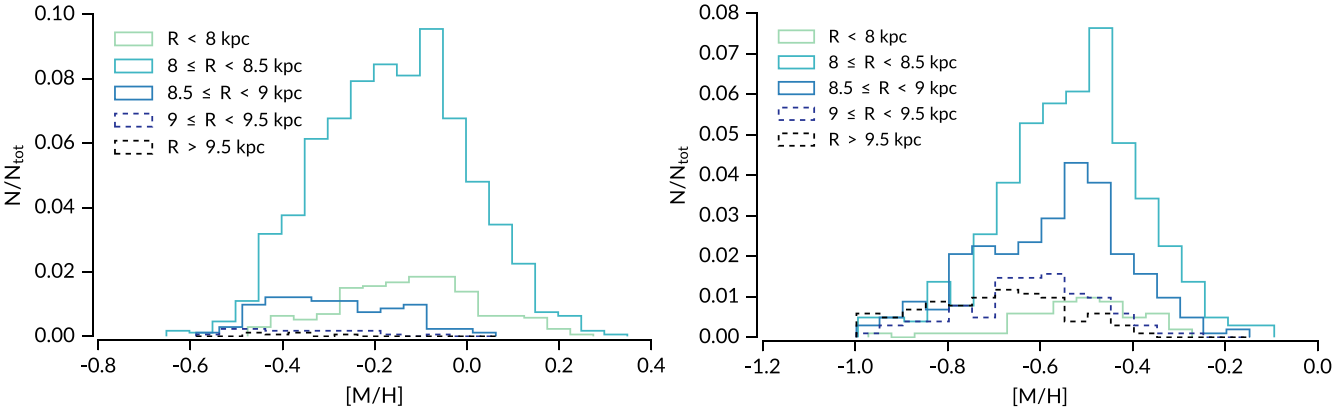

Figure 11. Radial distribution of the thin (low-α) and thick (high-α) discs, after correcting for selection effects. Left-hand panel: the thin disc's mean metallicity changes rapidly as a function of radial distance. This is due to both the radial metallicity gradient observed in the thin disc, and that the average vertical height increases with increasing radial distance. Right-hand panel: The thick disc, on the other hand, does not show a strong change in shape nor median value with radial distance.

pilot and main survey selections. The distances, on the other hand, are very different for the pilot and main surveys. The main survey is biased against stars more distant than 1.5 kpc, especially at lower metallicities. The pilot survey observes relatively more distant (and thus larger $|z|$) stars as intended. In addition, the pilot survey colour and magnitude limit particularly targeted red clump stars, which primarily contributed to the second peak in its selection function.

The relative ratios obtained from this population synthesis method are dependent on the choice of stellar models and IMFs; however, we note that we are only using these numbers in the relative sense, to gauge the importance of one star compared to another. In this sense, we do not expect the selection effects to change qualitatively.

4.2 Effects of bias correction

The final weight is determined by combining the fraction from field selection bias and the isochrone population synthesis. Since the fraction indicates how likely a star is observed, the weights are computed as

$$w_{\rm final} = \frac{1}{w_{\rm field} \times w_{\rm isochrone}}$$

so that stars less likely to be observed are given higher weights.

Overall, the corrections mean that more metal-poor and distant stars are weighted more heavily. Effects of the weights on the [M/H] and $|z|$ distributions are shown in Fig. 10.

4.3 Halo contamination

To assess the halo contamination in our low- and high-α samples, we used the GALAXIA code (Sharma et al. 2011), based on the *Besançon* models (Robin et al. 2003) to synthesize the stellar population within our observed region. We applied the same colour–magnitude limits (in 2MASS J, $K_{\rm s}$ photometry as shown in Fig. 1) for the pilot and main survey samples separately. The simulation shows that within our metallicity range ($-1 \leq$ [M/H] ≤ 0.4), the contamination of halo stars is extremely small, at 0.5 per cent for both of the pilot and main surveys. Therefore, any effects of halo stars on our results would be negligible.

5 METALLICITY PROFILES

5.1 Radial metallicity profiles

In Fig. 11, we show the MDF of the thin and thick discs in radial distance bins of 500 pc. Within the small range that we cover, no

Table 1. The mean (and standard error), dispersion, and skewness of the metallicity distributions at different radial bins for the low-α population.

Radial range	Mean [M/H]	Standard deviation	Skewness
$R < 8$ kpc	-0.12 ± 0.01	0.15	$+0.01 \pm 0.02$
$8 \leq R < 8.5$ kpc	-0.16 ± 0.004	0.16	-0.02 ± 0.01
$8.5 \leq R < 9$ kpc	-0.30 ± 0.01	0.13	$+0.30 \pm 0.02$
$9 \leq R < 9.5$ kpc	-0.37 ± 0.03	0.17	$+1.50 \pm 0.07$
$R > 9.5$ kpc	-0.42 ± 0.05	0.13	-0.30 ± 0.07

Table 2. The mean (and standard error), dispersion, and skewness of the metallicity distributions at different radial bins for the high-α population.

Radial range	Mean [M/H]	Standard deviation	Skewness
$R < 8$ kpc	-0.52 ± 0.02	0.13	-0.79 ± 0.04
$8 \leq R < 8.5$ kpc	-0.53 ± 0.01	0.15	-0.27 ± 0.01
$8.5 \leq R < 9$ kpc	-0.57 ± 0.01	0.15	-0.26 ± 0.02
$9 \leq R < 9.5$ kpc	-0.61 ± 0.01	0.14	-0.36 ± 0.03
$R > 9.5$ kpc	-0.70 ± 0.02	0.15	-0.07 ± 0.04

metallicity gradient is observed for the thick disc. The MDF remains constant in shape and median value across all radial distances up to 9 kpc, which is consistent with Hayden et al. (2015). Beyond 9 kpc, we notice that the MDF skews slightly towards more metal-poor values, but we interpret this as an effect caused by observing progressively larger median $|z|$ as we move further from the Galactic Centre (see Fig. 2) rather than the thick disc having a radial metallicity gradient.

For the low-α population, we observe only a small number of stars at radial distances further than 9 kpc. The distribution is roughly Gaussian at all locations, but skews towards metal-poor with increasing R. In Fig. 2, it is evident that the majority of α-poor stars (thin disc) are confined to the plane. At $R_{GC} = 8.5$ kpc, most of the stars lie above $|z| = 1$ kpc, so here we are likely to be observing only the metal-poor tail of the thin disc. The shift towards lower metallicity at large R is likely due to the radial metallicity gradient of the thin disc (Cheng et al. 2012; Genovali et al. 2014; Hayden et al. 2015), and the vertical gradient discussed in the next section.

We provide the median, standard deviation, and skewness of each radial bin of each population in Tables 1 and 2. These support our conclusions that the MDFs of both populations within our R_{GC} range are close to Gaussian, and that there is little change in the mean metallicity and shape of the high-α population. We caution that the statistics is more uncertain for bins $R_{GC} > 9$ kpc of the low-α population due to the small sample size.

5.2 Vertical metallicity profiles

The vertical gradients were measured using an orthogonal linear least-squares regression to all data points, taking into account each data point's uncertainties in [M/H] and vertical height. Each point is then weighted by the selection bias correction described in Section 4. We do this by decreasing the uncertainty of each data point by the square root of the correction factor. In this section, we report the gradients measured for the disc as a whole, and for each defined α sub-population. The gradients measured are summarized in Table 3.

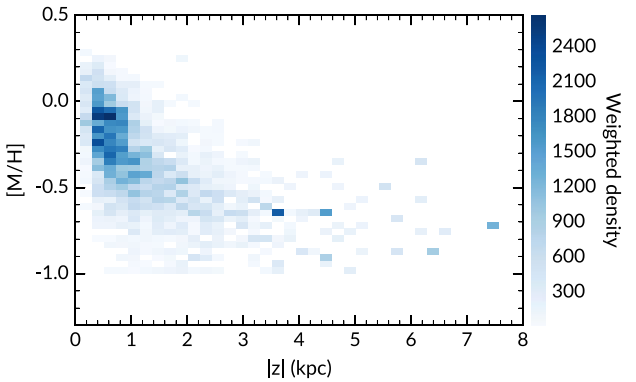

Figure 12. Variation of metallicity with distance from the Galactic plane for all stars independently of their α assignment (the 'transition' stars mentioned in Section 3.3 are also included). The density was weighted using bias correction fractions described in Section 4. The metallicity decreases smoothly with increasing height; however, the gradient appears to flatten at $|z| = 2$ kpc.

Fig. 12 shows a density plot of the metallicity as a function of height above the plane for all stars, including those that were omitted from the individual α-subpopulation, as explained in Section 3.3. The density was weighted to correct for selection biases using relative fractions described in Section 4. We observe that the metallicity decreases smoothly as $|z|$ increases. The vertical gradient for the disc overall is $\mathrm{d[M/H]/d}z = -0.22 \pm 0.01$ dex kpc^{-1}, and appears to flatten at larger $|z|$, from about $|z| = 2$ kpc. The gradient value is in good agreement with overall disc gradients measured by Schlesinger et al. (2014) for a sample of volume-complete SEGUE dwarfs.

For each of the sub-populations, we also found a metallicity gradient, as shown in Fig. 13. Overplotted in each panel are averaged values of metallicity at different $|z|$ bins for clarity, but these binned values have no effect on the data fitting. We discuss the vertical gradients below.

5.2.1 *The low-α population*

The low-α population, or thin disc, is known to have a radial metallicity gradient $\mathrm{d[M/H]/d}R$ of ≈ -0.08 dex kpc^{-1}, which flattens at progressively higher $|z|$ (Cheng et al. 2012; Hayden et al. 2014). The radial metallicity gradient can be seen in the left-hand panel of Fig. 11, where the median metallicity shifts to lower values at larger R_{GC}. The small R_{GC} range that we cover does not allow us to reliably measure radial metallicity gradients, so we corrected for this effect by estimating the metallicity of each star at $R = 8$ kpc using radial gradients specified in Cheng et al. (2012) for height bins $0.25 < |z| < 0.5$, $0.5 < |z| < 1$, and $1 < |z| < 1.5$ kpc. The

Table 3. Summary of measured vertical gradients, and intercepts at $|z| = 0$ for disc metallicity and α-abundances.

Population	d[M/H]/dz dex kpc^{-1}	$\sigma_{\mathrm{d[M/H]/d}z}$	$[\mathrm{M/H}]_{(z=0)}$ dex	$\sigma_{[\mathrm{M/H}](z=0)}$	d[α/M]/dz dex kpc^{-1}	$\sigma_{\mathrm{d}[\alpha/\mathrm{M}]/\mathrm{d}z}$	$[\alpha/\mathrm{M}]_{(z=0)}$ dex	$\sigma_{[\alpha/\mathrm{M}](z=0)}$
low-α	-0.18	0.01	-0.02	0.01	$+0.008$	0.002	0.06	0.002
high-α	-0.058	0.003	-0.47	0.01	$+0.007$	0.002	0.20	0.003
All stars	-0.22	0.01	-0.08	0.01	$+0.038$	0.001	0.08	0.002

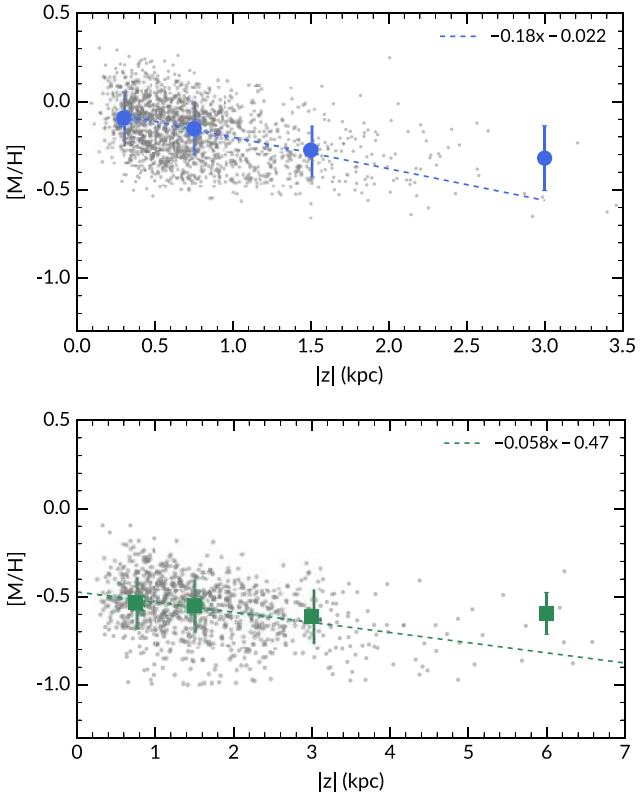

Figure 13. Variation of metallicity with distance from the Galactic plane for each α sub-population. Top panel: the thin disc has a steep negative gradient, which is consistent with what many authors have observed previously. Bottom panel: the thick disc has a shallower gradient. The trends are fitted over grey data points, overplotted are averaged values of four height bins and their one sigma error bars. It is important to note that the binned values were not used in the gradient fitting.

data set of Cheng et al. (2012) did not extend beyond $|z| = 1.5$ kpc, so for all heights above this value, we assumed the same radial gradient as at $1 < |z| < 1.5$. Overall, the radial gradient correction caused a change of -0.01 dex kpc^{-1} in the vertical gradient. The final weighted vertical gradient of the low-α population d[M/H]/dz $= -0.18 \pm 0.01$ dex kpc^{-1}.

Studies that were conducted prior to recent large spectroscopic surveys typically reported steeper negative gradients than our value. Bartašiūtė et al. (2003) separated thin disc stars by rotational lag and measured -0.23 ± 0.04 dex kpc^{-1}. Marsakov & Borkova (2006) used both space velocities and orbital eccentricities restrictions to select thin disc stars and reported a gradient of -0.29 ± 0.06 dex kpc^{-1}. It is highly likely that separating the thin disc purely based on kinematics would result in contamination of thick disc stars, which explains why these gradients are in agreement with our overall disc gradient, but steeper than the gradient of the low-α population.

Few studies of disc vertical metallicity gradients separated the thin/thick disc using chemistry. The only recent studies that identified the thin disc by their α-abundances are Schlesinger et al. (2014) (SEGUE), Hayden et al. (2014) (APOGEE), and Mikolaitis et al. (2014) (*Gaia*-ESO). Hayden et al. (2014) found a low-α gradient of -0.21 ± 0.02 dex kpc^{-1}at the solar circle for the APOGEE DR10 sample, which is slightly steeper than our value. Hayden et al. (2014) also correct for the radial metallicity gradient, using values similar to that of Cheng et al. (2012) used here. The small discrepancy could arise from our different definitions of the thin disc, as Hayden et al. (2014) made a straight-line cut at [α/M] $=$ 0.18. In fig. 6 of Hayden et al. (2014), their low-α population extends to [M/H] $= -2$ dex while ours extends to only [M/H] $= -0.6$ dex. The low-α, very metal-poor stars seen in APOGEE data could belong to the halo (Nissen & Schuster 2010; Adibekyan et al. 2013), and this contamination would steepen the gradient.

Schlesinger et al. (2014) also computed a gradient for the low-α population of SEGUE dwarfs. They measured, for the disc as a whole, a vertical metallicity gradient of $-0.24^{+0.04}_{-0.05}$ dex kpc^{-1}, which is in agreement with our measurement. However, their low-α population has a gradient consistent with zero: d[M/H]/d$z = -0.01^{+0.09}_{-0.06}$ dex kpc^{-1}. However, their intermediate α sub-population with $0.2 <$ [α/M] < 0.3 has d[M/H]/dz $= -0.17^{+0.08}_{-0.07}$ dex kpc^{-1}, which agrees with our low-α metallicity gradient. We thus conclude that the discrepancy between our result and that of Schlesinger et al. (2014) is largely due to the chemical separation criteria (also see Ciucă et al. 2018, who found an age-dependence for the thin disc vertically metallicity gradient, such that the youngest population has a flatter gradient).

Mikolaitis et al. (2014) measured a slightly shallower gradient of d[M/H]/d$z = -0.11 \pm 0.01$ for *Gaia*-ESO dwarfs and giants. The *Gaia*-ESO sample is more metal-poor overall, and Mikolaitis et al. (2014) separated thick disc stars by the location of underdensities in their [Mg I/M] histograms (their fig. 3). The dividing line is at different values of [Mg I/M] for different metallicity regimes. In fig. 10 of Mikolaitis et al. (2014), it is clear that their sample is biased against metal-rich stars, such that there are very few stars with [M/H] > 0 (also see Stonkutė et al. 2016).

5.2.2 *The high-α population*

The vertical metallicity distribution of the thick-disc (high-α) stars is relatively flat compared to the low-α population, at -0.058 ± 0.003 dex kpc^{-1}. Several authors have measured the vertical gradient for the thick disc, using different methods to define this population. Earlier studies, such as Gilmore et al. (1995) and Prieto et al. (2006), reported no vertical metallicity gradient in the thick disc (Prieto et al. 2006 quoted an upper limit of d[M/H]/d$z = 0.03$ dex kpc^{-1}). More recently, Boeche et al. (2014) concluded that the vertical metallicity gradient of the thick disc is consistent with zero, based on a sample of RAVE giants. However, other studies, using a combination of metallicity or kinematics to separate the thick disc, have reported a shallow metallicity gradient.

Katz et al. (2011) observed sub-giants at two lines of sight: (l, b) $= (51^\circ, 80^\circ)$ and $(5^\circ, 46^\circ)$ at low resolution. Their MDFs show signs of bimodality, and the thick disc was defined as stars centred around [M/H] ≈ -0.5 dex. The vertical gradient measured by Katz et al. (2011) is -0.068 ± 0.009 dex kpc^{-1}, consistent with our value.

Ruchti et al. (2011) observed a number of metal-poor thick disc candidates at high resolution using the MIKE, FEROS and UCLES spectrographs ($\lambda/\Delta\lambda \approx 35\,000$–$45\,000$). They classified their stars based on a Monte Carlo simulation of space motion U, V, W, assuming Gaussian errors on the velocities and distances. By further restricting their α-enhanced sample with thick disc kinematics to metal-poor stars only ([M/H] ≤ -1.2), they avoid most thin disc contamination. The measured gradient is -0.09 ± 0.05 dex kpc^{-1}, which also agrees with our results.

Kordopatis et al. (2011) observed stars using the VLT/GIRAFFE spectrograph ($\lambda/\Delta\lambda \approx 6500$) at almost the same Galactic longitude as the GALAH pilot survey ($\ell = 277^\circ$), and the same latitude as our highest fields ($b = 47^\circ$). They reported a gradient of -0.14 ± 0.05

dex kpc^{-1} for stars at heights $1 < |z| < 4$ kpc, where the thick disc is dominant, which does not agree with our result. Selecting the thick disc based only on height above the plane will certainly include thin disc contaminants and thus cause their gradient to be steeper.

Chen et al. (2011) selected a sample of SDSS stars at $1 < |z| < 3$ kpc to represent the thick disc and measured a vertical gradient of -0.22 ± 0.07 dex kpc^{-1}. From the separation by chemistry shown in this paper and elsewhere, thin disc stars exist at $|z|$ up to at least 2 kpc, so a thick disc definition based on vertical height alone is not very accurate. Chen et al. (2011) provides another estimate of -0.12 ± 0.01 dex kpc^{-1} for the gradient after they have modelled and subtracted thin disc contaminants using the Besançon model, which is closer to our value. However, neither of these thick disc vertical metallicity gradients is in agreement with our value.

Comparing our measurement of the vertical gradient for the high-α population with the gradient from the APOGEE DR10 (Hayden et al. 2014) reveals a large discrepancy, as they found a steep negative gradient of -0.26 ± 0.02 dex kpc^{-1} at the solar circle. However, APOGEE DR10 suffered from systematic errors in the α abundance determinations, particularly for cooler stars. This may have caused errors in their measured abundance gradients, and thus the discrepancy between our results (Hayden, private communication). The gradient measured for the same stars using APOGEE DR13 is -0.09 ± 0.01 dex kpc^{-1}, which, although not in agreement with our result, is much more similar (Hayden, private communication). Gradients measured for APOGEE stars are restricted to $|z| \leq 2$ kpc, which could explain why their measurement is steeper than ours, as we see that the vertical metallicity gradient flattens at larger heights.

5.3 The effects of excluding 'transition' stars

As mentioned in Section 3.3, we omitted all stars that lie between the low- and high-α populations in terms of abundances and radial velocities so to minimize possible contaminations. In a purely chemical separation, however, they would contribute to the vertical gradients. We explored the effects of excluding them by separating the two populations by [α/M] only, making a cut at [α/M] = 0.15, where the 'gap' is located, and repeated our analysis of the gradients. As expected, the vertical metallicity gradients for both sub-populations steepened compared to our probability-based thin/thick disc separation using the [M/H]–[α/M]–RV distribution described in Section 3.3. The low-α population changes to d[M/H]/d$z = -0.21 \pm 0.01$, and the high-α population to d[M/H]/d$z = -0.11 \pm 0.004$. For the high-α population, we would then be in better agreement with APOGEE DR13 and Kordopatis et al. (2011).

6 [α/M] PROFILES

Within the 1.5 kpc R_{GC} range of our sample, we do not observe any significant radial changes in [α/M] for either of the defined populations. Studies of the high-α population's radial abundance gradients show that there is no variation, but there may be small positive radial [α/M] gradients in the low-α population (e.g. Bergemann et al. 2014; Mikolaitis et al. 2014). Genovali et al. (2015), however, found a negative radial abundance gradient for the α-element Ca. Boeche et al. (2014) also found modest radial gradients for the α-elements. The fact that we do not observe a radial abundance gradient in the low-α population is likely due to our limited radial coverage, which prevents us from assessing [α/M] variation with R_{GC}.

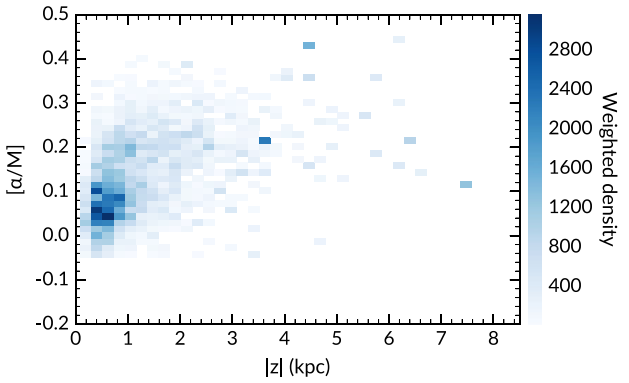

Figure 14. Variation of [α/M] with distance from the Galactic plane for all stars. The density is weighted by selection bias fractions as described in Section 4. The over densities at high $|z|$ are due to a few data points with large weights. Unlike metallicity, [α/M] does not vary smoothly with increasing height. There appears to be a break in the distribution at $|z| \approx 1$ kpc.

The vertical α-abundance profile of the entire sample is shown in Fig. 14, presented as a density plot similar to Fig. 12. The median [α/M] increases as a function of height, as noted previously by Schlesinger et al. (2014) and Mikolaitis et al. (2014). However, unlike the metallicity, we find that the α-abundance profile does not vary smoothly with $|z|$. The α-abundance vertical gradient for the entire disc is d[α/M]/d$z = 0.038 \pm 0.001$ dex kpc^{-1}. For the low- and high-α populations, the [α/M] vertical gradients are both slightly positive, as shown in Fig. 15. The gradients are d[α/M]/d$z = 0.008 \pm 0.002$ dex kpc^{-1} for the low-α population, and d[α/M]/d$z = 0.007 \pm 0.002$ dex kpc^{-1} for the high-α population. As in Section 5.3 above, we also analysed the two α populations with the 'transition stars' included. This did not change the slope measured for the low-α population, but increased the slope of the high-α population to d[α/M]/d$z = 0.014 \pm 0.001$ dex kpc^{-1}, which is higher than the value measured without transition stars. The transition stars contribute primarily at low $|z|$ ($\leq$1 kpc), which is why their addition affected the high-α population more: As defined in Section 3.3, this population is mainly located at $|z| \geq 1$ kpc.

For the high-α population, Ruchti et al. (2011) showed that individual α-abundances [Mg/Fe] and [Si/Fe] have vertical gradients 0.03 ± 0.02 and 0.02 ± 0.01 dex kpc^{-1}, respectively. Meanwhile, the vertical abundance gradients of [Ca/Fe] and [Ti I,II/Fe] decrease to -0.01 ± 0.01 and -0.02 ± 0.02 dex kpc^{-1}. While we do not have α-enhanced stars with [M/H] < -1 as in their study, this result is in agreement with the flat gradients we observe. Mikolaitis et al. (2014) also provide vertical gradients for the averaged [α/M] abundances, as well as vertical gradients for individual α-elements using *Gaia*-ESO iDR1. Mikolaitis et al. (2014) found similar vertical abundance profiles for the low- and high-α stars. Both populations have averaged and individual vertical α-abundance gradients of 0.04–0.05 dex kpc^{-1}, with errors <0.01 dex kpc^{-1}. These values are not in agreement with our measured vertical gradient for the α sub-populations, as we find that both populations have rather flat abundance distributions as a function of height. However, these results are similar to the gradient we derived for the disc overall. The differences could have arisen from the lack of correction for selection biases in Mikolaitis et al. (2014) and the different abundance scales of the *Gaia*-ESO and GALAH surveys. The [Mg/Fe] histograms shown in fig. 3 of Mikolaitis et al. (2014) show that

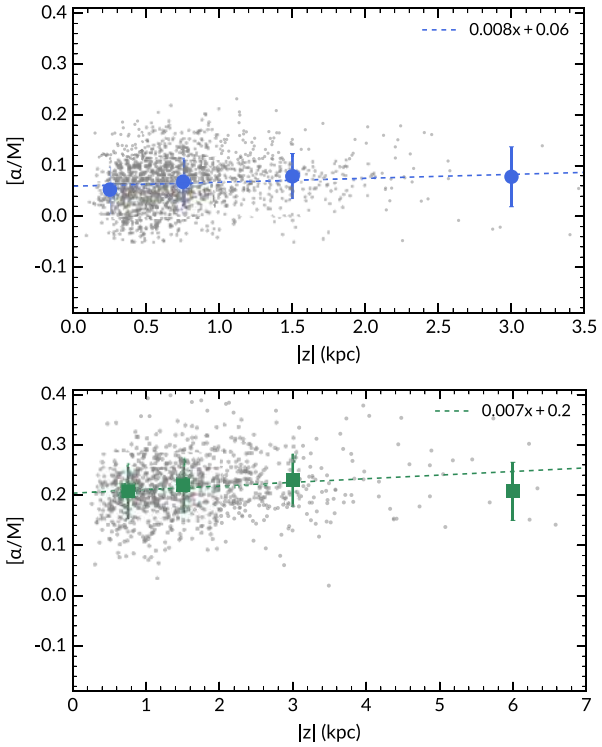

Figure 15. Variation of [α/M] with distance from the Galactic plane for each of the high- and low-α population. Top panel: vertical abundance gradient for the low-α stars. Bottom panel: vertical abundance gradient of the high-α stars. Both populations show a flat-positive trend. The high-α population shows a higher dispersion in [α/M] values. The trends are fitted over grey data points, overplotted are averaged values of four height bins and their one sigma error bars. Note that the binned values were not used in the gradient fitting.

Gaia-ESO iDR1 has a larger spread in their abundances compared to GALAH (cf. Fig. 5).

An important point to consider is the dependence of [α/M] on [M/H], and the correlation of the latter with respect to vertical height $|z|$. At greater heights above the plane, observed stellar populations become more metal-poor (Fig. 12), and these stars are typically more α-enhanced. The positive α-gradient over the entire disc is therefore reflective of the fact that more metal-poor, high-α stars become dominant at large heights. For each of the α sub-populations as defined in Fig. 8, however, the correlation between [α/M] and [M/H] is rather flat, which means that the small positive gradients we measured are intrinsic to these sub-populations.

7 DISCUSSION

The process(es) that created the thick disc have been a central point of discussion in Galactic studies. The very definition of the thick disc has changed since first proposed by Gilmore & Reid (1983), and here we refer to the 'thick disc' as the overall more α-enhanced population as defined in Section 3.3 using both chemical and kinematical information. In Section 1, we outlined the main scenarios that have been proposed for thick disc formation, and in this section we interpret our results in the context of these scenarios.

In summary, the vertical metallicity and abundance profiles of the disc shows the following:

(1) The disc overall has a steep negative vertical metallicity gradient.

(2) The low-α population has a similar vertical metallicity gradient to the full disc.

(3) The high-α population, on the other, has a much flatter vertical metallicity gradient.

(4) The α-abundance ratio increases with height in general. At larger heights, only the high-α population is present.

(5) Neither the high nor low-α sub-population shows a significant vertical α abundance ratio gradient.

The vertical metallicity gradient in the high-α population is in contrast with predictions of the direct satellite accretion scenario proposed by Abadi et al. (2003) and the fast internal evolution model of Bournaud et al. (2009). While both of these scenarios could result in a chemically distinct thick disc, they also predict a uniform vertical metallicity distribution, or a lack of vertical metallicity gradient. Brook et al. (2004, 2005) proposed that the thick disc formed via merging of gas-rich clumps at high redshift, prior to the formation of the thin disc. Their model predicts an old, α-enhanced thick disc that matches observations. However, their thick disc also shows no vertical metallicity gradient, in contrast to our results.

The heating of an existing disc by small satellite mergers can create a thick-disc like vertical structure (e.g. Quinn & Goodman 1986; Quinn et al. 1993; Kazantzidis et al. 2008; Villalobos & Helmi 2008). The vertical metallicity gradient of the existing disc could be preserved in the thick disc; however, this can also be affected by the interplay between radial migration and radial metallicity gradients (e.g. Kawata et al. 2018). Bekki & Tsujimoto (2011) modelled the kinematics and chemistry of stars formed by minor mergers in detail, and showed that a fast star formation rate in the thick disc results in α-enhanced stars. The steep vertical metallicity gradient of the pre-existing disc flattens over time, but qualitatively it is steeper in the inner Galaxy, consistent with the observations of Hayden et al. (2014). However, the final thick disc gradient is essentially flat at the solar circle, which is not what we observe. Furthermore, disc flaring is expected in such a heating scenario. For the high-α stars, Bovy et al. (2016) did not observe any flaring in their MAPs. However, Minchev et al. (2015, 2016) argued that mono-age populations always flare in their cosmological simulations, and MAPs are not necessarily co-eval. Based on APOGEE abundances and calibrated ages, [7] Mackereth et al. (2017) found that mono-age α-enhanced populations do show some flaring, albeit with a smaller amplitude compared to the low-α population. Further observational and model constraints from stellar ages and flaring of the high-α stars are thus needed to understand the importance of minor mergers in thick disc formation.

The secular radial migration (Sellwood & Binney 2002) process was proposed by Schönrich & Binney (2009) as the sole explanation for the thick disc (but this remains controversial, see e.g. Minchev et al. 2012; Vera-Ciro et al. 2014). Stars in the inner galaxy are formed fast and migrated outwards to create the α-enhanced population at large scaleheights. Since radial migration is more likely to affect older stars, a negative vertical metallicity gradient, and a positive [α/M] gradient are expected. Schönrich & McMillan (2017) obtain $\mathrm{d[M/H]/d}z \approx -0.2$ dex kpc^{-1}for the full nearby disc in their analytical model (which included inside-out disc formation), in agreement with our observations. Loebman et al. (2011) also reported a similar vertical gradient of ≈ -0.18 dex kpc^{-1}in their *N*-body simulation with extensive radial migration. Both of these values are consistent with our measurements of the

[7] Ages from Martig et al. (2016a), calibrated on APOGEE DR12 C and N abundance ratios.

full disc and low-α population, even though Loebman et al. (2011) did not calibrate their model to reproduce the Milky Way.

Radial migration signatures are observed in the MDF of disc stars at different Galactocentric radii. Hayden et al. (2015) observed that at small heights above the plane, the skewness of MDFs changes from negative in the outer galaxy (skewed towards metal-poor stars) to positive (skewed towards metal-rich stars) in the inner galaxy. In contrast, the high-α population's MDF remains constant at all locations. Loebman et al. (2016) showed that these observations can be qualitatively explained by radial migration in their simulation. The change in skewness of the disc MDFs at different radii could be due to an increased fraction of migrated stars beyond $\approx$5 kpc, such that more metal-rich stars are migrated to larger $R_{\rm GC}$. As the high-α stars formed within a small region and a few Gyrs in a well mixed environment, their chemical content is similar and thus the MDF remains constant at all Galactic locations. Loebman et al. (2016) found a small vertical metallicity gradient in their simulated high-α population of ≈ -0.03 dex kpc^{-1}. This is half the value observed in our study. Further investigation of the vertical metallicity and abundance gradients for the high-α stars in radial migration models will help to determine the extent to which it affects this population.

Bird et al. (2013) was able to produce a Milky Way-like galaxy with an old, vertically extended population much like the Galactic thick disc using the 'Eris' cosmological simulation suite. The effects of the active merger phase at early times (redshift > 3), secular heating, and radial migration on the present-day galaxy were examined. Bird et al. (2013) found that stars born during the merger phase have larger scaleheights and shorter scalelengths, and younger populations form progressive thinner and longer structures. This gradual transition from a kinematically hot and thick disc to a colder, thinner disc was dubbed 'upside down' formation (see also Samland & Gerhard 2003). Interestingly, secular heating and radial migration did not have a large impact on the final properties of each co-eval population. Rather, the trends are established at formation, suggesting that the thick disc-like component was born thick. Similarly, Stinson et al. (2013) and Brook et al. (2012) concluded that their α-enhanced, older populations were born kinematically hot, and that the early disc settles into a thin component. The settling process of the galaxies and fast formation of the old, α-enhanced, and vertically extended populations in these simulations could produce the vertical metallicity and abundance profiles observed in this work. It was shown by Wisnioski et al. (2015) that the observed velocity dispersion of Hα gas in galaxies at high redshift decreases with time, providing further indication that disc galaxies were born thick at redshifts of $z = 1 - 2$.

While the cosmological models mentioned above heavily rely on the condition that disc galaxies like the Milky Way had a quiescent merger history, there is observational evidence that this may be true for the Galaxy (Ruchti et al. 2015; Casagrande et al. 2016). However, the metallicity and α-abundance gradients in these simulations have not been studied in detail.

Although we observe an overall continuity in the vertical metallicity profile, we see two distinct α-enhancement tracks as a function of $|z|$, which have implications for the star formation history of the disc. Haywood et al. (2013, 2016) proposed two different star formation epochs for the high- and low-α stars. By comparing their chemical evolution model (Snaith et al. 2015) with APOGEE data, Haywood et al. (2016) proposed that the star formation rate dropped significantly at ages of 10 Gyr before increasing again at about 7 Gyr to a lower maximum value. This could indicate the transition between thick to thin disc formation. However, the authors note that due to the strict continuity of the stellar abundances, the gas supply must not have decreased during this period of time. Similarly, Brook et al. (2012) found that the star formation rate decreased slightly at around 7 Gyr, near the epoch of thin disc formation in their simulation. This idea was also explored by the two-infall model proposed by Chiappini, Matteucci & Gratton (1997), who argued for a decreased star formation rate between the epochs of halo-thick disc and thin disc formation, and proposed a shorter formation time-scale for the halo/thick disc of 1 Gyr. Future work that incorporate stellar ages (e.g. from the GALAH/K2 overlap) will be able to rigorously test these scenarios and provide additional constraints on the formation time-scale of the thick disc.

8 CONCLUSION

We have determined the vertical profiles of metallicity and α-abundances in the Galactic disc using data from the GALAH first internal data release. We analysed in total 3191 giants from the GALAH pilot and main surveys, extending up to 4 kpc in height above the plane, within a small range of Galactocentric distance ($7.9 \lesssim R_{\rm GC} \lesssim 9.5$ kpc). The precise metallicity and abundance measurements of GALAH allow us to reliably define 'thick' and 'thin' disc populations using chemistry and radial velocities. The GALAH magnitude limits in the estimated V-band translate to a dependency in $(J - K)$ colour and magnitudes. We corrected for the selection effects for targets from the pilot and main surveys separately by population synthesis using BaSTI isochrones.

The vertical metallicity gradient of the entire disc is -0.22 ± 0.01 dex kpc^{-1}, which is in agreement with recent estimates from large spectroscopic surveys such as SEGUE and APOGEE. The low-α population, or the thin disc, also exhibits a steep negative vertical metallicity gradient d[M/H]/d$z = -0.18 \pm 0.01$ dex kpc^{-1}. The more enhanced α population, which we identify as the thick disc, is found to have a shallower vertical gradient d[M/H]/dz of -0.058 ± 0.003 dex kpc^{-1}. We note again that our data do not probe the metal-poor extension of the thick disc; however, the vertical gradients observed here are similar in amplitude to those of previous studies. Overall, our results confirm some conclusions reached by earlier studies, despite differences in target selection, spatial coverage, and abundance scales. The discrepancies were likely caused by uncorrected selection effects in some cases, and the many different definitions in the literature of high-α, or thick disc stars.

As expected, [α/M] increases as a function of $|z|$, with the low-α population occupying lower heights on average. The vertical [α/M] profile at the solar circle shows that there are two overdensities, with the discontinuity most clearly seen around $|z| = 1$ kpc. We find that the both low- and high-α sub-populations have a flat vertical [α/M] gradient. Similarly, Ruchti et al. (2011) also found flat vertical gradients for individual α-abundances at the metal-poor end of the α-enhanced population. For the low-α population, the gradient can be explained by radial migration playing an important role in the evolution of the thin disc. The negative vertical metallicity gradient of the high-α population indicates that formation scenarios which produce uniform 'thick disc' vertical metallicity gradients are not responsible for its formation. The vertical [M/H] gradient observed in this work and elsewhere could have arisen from a settling phase of the disc as suggested by Samland & Gerhard (2003) and Bird et al. (2013), minor heating episodes such as in the models of Kazantzidis et al. (2008); Villalobos & Helmi (2008), or caused by radial migration (Schönrich & Binney 2009; Loebman et al. 2011). Mergers cause flaring of the disc, which is seen in the low-α population in the analysis of Bovy et al. (2016), but not in the high-α population. However, Mackereth et al. (2017) have since shown

that co-eval high-α populations do indeed show flaring, but much less than the low-α stars. On the other hand, the α-abundances of both sub-populations are distinct and nearly constant at all heights, indicating that they are formed in very different conditions.

Accurate distances and proper motion from *Gaia* DR2 will allow for an even more accurate and detailed analysis of the chemistry and kinematics of the high-α population, not only for the GALAH pilot survey but also the larger GALAH main sample. This will give us a clearer and more definitive picture of the formation and evolution of the Milky Way thick disc.

ACKNOWLEDGEMENTS

We thank Michael R. Hayden for helpful discussions regarding APOGEE results, and the anonymous referee for comments that improved the clarity of this manuscript. LD and MA acknowledge funding from the Australian Government through ARC Laureate Fellowship FL110100012. LD, KCF, and RFGW acknowledge support from ARC grant DP160103747. LC gratefully acknowledges support from the Australian Research Council (grants DP150100250, FT160100402). DMN was supported by the Allan C. and Dorothy H. Davis Fellowship. DS is the recipient of an Australian Research Council Future Fellowship (project number FT1400147). TZ acknowledges financial support from the Slovenian Research Agency (research core funding No. P1-0188). Part of this research was supported by the Munich Institute for Astro- and Particle Physics (MIAPP) of the DFG cluster of excellence 'Origin and Structure of the Universe'.

This publication makes use of data products from the Two Micron All Sky Survey, which is a joint project of the University of Massachusetts and the Infrared Processing and Analysis Center/California Institute of Technology, funded by the National Aeronautics and Space Administration and the National Science Foundation; and data products from the Wide-field Infrared Survey Explorer, which is a joint project of the University of California, Los Angeles, and the Jet Propulsion Laboratory/California Institute of Technology, funded by the National Aeronautics and Space Administration.

REFERENCES

Abadi M. G., Navarro J. F., Steinmetz M., Eke V. R., 2003, ApJ, 591, 499
Adibekyan V. Z., Santos N. C., Sousa S. G., Israelian G., 2011, A&A, 535, L11
Adibekyan V. Z. et al., 2013, A&A, 554, A44
Amarsi A. M., Asplund M., Collet R., Leenaarts J., 2015, MNRAS, 454, L11
Amarsi A. M., Asplund M., Collet R., Leenaarts J., 2016, MNRAS, 455, 3735
Anguiano B. et al., 2015, MNRAS, 451, 1229
Astraatmadja T. L., Bailer-Jones C. A. L., 2016, ApJ, 833, 119
Aumer M., Binney J., Schönrich R., 2016, MNRAS, 459, 3326
Bartašiūtė S., Aslan Z., Boyle R. P., Kharchenko N. V., Ossipkov L. P., Sperauskas J., 2003, Balt. Astron., 12, 539
Bekki K., Tsujimoto T., 2011, ApJ, 738, 4
Bensby T., Alves-Brito A., Oey M. S., Yong D., Meléndez J., 2011, ApJ, 735, L46
Bensby T., Feltzing S., Oey M. S., 2014, A&A, 562, A71
Bergemann M. et al., 2014, A&A, 565, A89
Bird J. C., Kazantzidis S., Weinberg D. H., Guedes J., Callegari S., Mayer L., Madau P., 2013, ApJ, 773, 43
Bland-Hawthorn J., Gerhard O., 2016, ARA&A, 54, 529
Boeche C. et al., 2014, A&A, 568, A71
Bournaud F., Elmegreen B. G., Martig M., 2009, ApJ, 707, L1
Bovy J., Rix H.-W., Hogg D. W., 2012a, ApJ, 751, 131
Bovy J., Rix H.-W., Liu C., Hogg D. W., Beers T. C., Lee Y. S., 2012b, ApJ, 753, 148
Bovy J., Rix H.-W., Schlafly E. F., Nidever D. L., Holtzman J. A., Shetrone M., Beers T. C., 2016, ApJ, 823, 30
Brook C. B., Kawata D., Gibson B. K., Freeman K. C., 2004, ApJ, 612, 894
Brook C. B., Gibson B. K., Martel H., Kawata D., 2005, ApJ, 630, 298
Brook C. B. et al., 2012, MNRAS, 426, 690
Brown A. G. A. et al., 2016, A&A, 595, A2
Burkert A., Truran J. W., Hensler G., 1992, ApJ, 391, 651
Burnett B., Binney J., 2010, MNRAS, 407, 339
Burstein D., 1979, ApJ, 234, 829
Casagrande L., Ramírez I., Meléndez J., Bessell M., Asplund M., 2010, A&A, 512, 54
Casagrande L., Schönrich R., Asplund M., Cassisi S., Ramírez I., Meléndez J., Bensby T., Feltzing S., 2011, A&A, 530, A138
Casagrande L., Aguirre V. S., Stello D., Huber D., Serenelli A. M., Cassisi S., Dotter A., 2014, ApJ, 787, 110
Casagrande L. et al., 2016, MNRAS, 455, 987
Chen Y. Q., Zhao G., Carrell K., Zhao J. K., 2011, AJ, 142, 184
Cheng J. Y. et al., 2012, ApJ, 752, 51
Chiappini C., Matteucci F., Gratton R., 1997, ApJ, 477, 765
Chiba M., Beers T. C., 2000, AJ, 119, 2843
Ciucă I., Kawata D., Lin J., Casagrande L., Seabroke G., Cropper M., 2018, MNRAS, 475, 1203
Comerón S., Salo H., Janz J., Laurikainen E., Yoachim P., 2015, A&A, 584, A43
Dalcanton J. J., Bernstein R. A., 2002, AJ, 124, 1328
Dalton G. et al., 2016, in Evans C. J., Simard L., Takami H., eds, Proc. SPIE Conf. Ser. Vol. 9908, Ground-Based and Airborne Instrumentation for Astronomy VI. SPIE, Bellingham, p. 99081G
de Jong R. D. et al., 2011, The Messenger, 145, 14
De Silva G. M. et al., 2015, MNRAS, 449, 2604
Dempster A. P., Laird N. M., Rubin D. B., 1977, J. R. Stat. Soc. B, 39, 1
Dierickx M., Klement R., Rix H.-W., Liu C., 2010, ApJ, 725, L186
Drimmel R., Spergel D. N., 2001, ApJ, 556, 181
Edvardsson B., Andersen J., Gustafsson B., Lambert D. L., Nissen P. E., Tomkin J., 1993, A&A, 275, 101
Forbes J., Krumholz M., Burkert A., 2012, ApJ, 754, 48
Fuhrmann K., 2008, MNRAS, 384, 173
Furhmann K., Chini R., Kaderhandt L., Chen Z., 2016, MNRAS, 464, 2610
Genovali K. et al., 2014, A&A, 566, A37
Genovali K. et al., 2015, A&A, 580, A17
Gilmore G., Reid N., 1983, MNRAS, 202, 1025
Gilmore G., Wyse R. F. G., Jones J. B., 1995, AJ, 109, 1095
Gilmore G., Wyse R. F. G., Norris J. E., 2002, ApJ, 574, L39
Gilmore G. et al., 2012, The Messenger, 147, 25
Gratton R. G., Carretta E., Matteucci F., Sneden C., 2000, A&A, 358, 671
Grevesse N., Asplund M., Sauval A. J., 2007, Space Sci. Rev., 130, 105
Gustafsson B., Edvardsson B., Eriksson K., Jorgensen U. G., Nordlund A., Plez B., 2008, A&A, 486, 951
Hayden M. R. et al., 2014, AJ, 147, 116
Hayden M. R. et al., 2015, ApJ, 808, 132
Haywood M., 2008, MNRAS, 388, 1175
Haywood M., Di Matteo P., Lehnert M. D., Katz D., Gómez A., 2013, A&A, 560, A109
Haywood M., Di Matteo P., Snaith O., Lehnert M. D., 2015, A&A, 579, A5
Haywood M., Lehnert M. D., Di Matteo P., Snaith O., Schultheis M., Katz D., Gomez A., 2016, A&A, 589, 17
Heiter U., Jofré P., Gustafsson B., Korn A. J., Soubiran C., Thévenin F., 2015, A&A, 582, A49
Huber D. et al., 2017, ApJ, 844, 102
Ibata R., Mouhcine M., Rejkuba M., 2009, MNRAS, 395, 126
Jofré P. et al., 2014, A&A, 564, A133
Jurić M. et al., 2008, ApJ, 673, 864
Katz D., Soubiran C., Cayrel R., Barbuy B., Friel E., Bienaymé O., Perrin M., 2011, A&A, 525, A90

Kawata D., Grand R. J. J., Gibson B. K., Casagrande L., Hunt J. A. S., Brook C. B., 2017, MNRAS, 464, 702
Kawata D. et al., 2018, MNRAS, 473, 867
Kazantzidis S., Bullock J. S., Zentner A. R., Kravtsov A. V., Moustakas L. A., 2008, ApJ, 688, 254
Kordopatis G. et al., 2011, A&A, 535, A107
Kordopatis G., Wyse R. F., Chiappini C., Minchev I., Anders F., Santiago B., 2017, MNRAS, 467, 469
Kos J. et al., 2017, MNRAS, 464, 1259
Lind K., Bergemann M., Asplund M., 2012, MNRAS, 427, 27
Loebman S. R., Roškar R., Debattista V. P., Ivezić Ž., Quinn T. R., Wadsley J., 2011, ApJ, 737, 8
Loebman S. R., Debattista V. P., Nidever D. L., Hayden M. R., Holtzman J. A., Clarke A. J., Ro R., Valluri M., 2016, ApJ, 818, L6
Mackereth J. T. et al., 2017, MNRAS, 471, 3057
Majewski S. R., Zasowski G., Nidever D. L., 2011, ApJ, 739, 25
Majewski S. R. et al., 2017, AJ, 154, 94
Marigo P. et al., 2017, ApJ, 835, 77
Marsakov V. A., Borkova T. V., 2006, Astron. Lett., 32, 376
Martell S. L. et al., 2017, MNRAS, 465, 3203
Martig M. et al., 2016a, MNRAS, 456, 3655
Martig M., Minchev I., Ness M., Fouesneau M., Rix H.-W., 2016b, ApJ, 831, 139
Mashonkina L., Gehren T., Travaglio C., Borkova T., 2003, A&A, 397, 275
Matteucci F., François P., 1989, MNRAS, 239, 885
Michalik D., Lindegren L., Hobbs D., 2015, A&A, 574, A115
Mikolaitis Š. et al., 2014, A&A, 572, A33
Minchev I., Famaey B., 2010, ApJ, 722, 112
Minchev I., Famaey B., Quillen A. C., Dehnen W., Martig M., Siebert A., 2012, A&A, 548, A127
Minchev I., Martig M., Streich D., Scannapieco C., de Jong R. S., Steinmetz M., 2015, ApJ, 804, L9
Minchev I., Steinmetz M., Chiappini C., Martig M., Anders F., Matijevic G., Jong R. S. D., 2016, ApJ, 834, 27
Nemec J. M., Nemec A. F. L., 1993, AJ, 105, 1455
Ness M., Hogg D. W., Rix H.-W., Ho A. Y. Q., Zasowski G., 2015, ApJ, 808, 16
Nissen P. E., Schuster W. J., 2010, A&A, 511, L10
Norris J., 1987, ApJ, 314, L39
Ojha D. K., 2001, MNRAS, 322, 426
Pedregosa F. et al., 2011, J. Mach. Learn. Res., 12, 2825
Pietrinferni A., Santi C., Salaris M., Castelli F., 2004, ApJ, 612, 168
Piskunov N., Valenti J. A., 2017, A&A, 597, A16
Prieto C. A., Beers T. C., Wilhelm R., Newberg H. J., Rockosi C. M., Yanny B., Lee Y. S., 2006, ApJ, 636, 804
Prochaska J. X. et al., 2000, AJ, 120, 2513
Quinn P. J., Goodman J., 1986, ApJ, 309, 472
Quinn P. J., Hernquist L., Fullagar D. P., 1993, ApJ, 403, 74
Rahimi A., Carrell K., Kawata D., 2014, RA&A, 14, 1406
Recio-Blanco A. et al., 2014, A&A, 567, A5
Robin A. C., Reylé C., Derrière S., Picaud S., 2003, A&A, 409, 523
Rojas-Arriagada A. et al., 2016, A&A, 586, A39
Roškar R., Debattista V. P., Quinn T. R., Wadsley J., Lancashire C., Pr P., 2012, MNRAS, 426, 2089
Ruchti G. R. et al., 2011, ApJ, 737, 9
Ruchti G. R. et al., 2015, MNRAS, 450, 2874
Sales L. V. et al., 2009, MNRAS, 400, L61
Salpeter E. E., 1955, ApJ, 121, 161
Samland M., Gerhard O. E., 2003, A&A, 399, 961
Schlegel D. J., Finkbeiner D. P., Davis M., 1998, ApJ, 500, 525
Schlesinger K. J. et al., 2014, ApJ, 791, 112
Schönrich R., Binney J., 2009, MNRAS, 399, 1145
Schönrich R., McMillan P. J., 2017, MNRAS, 18, 1154
Sellwood J. A., Binney J., 2002, MNRAS, 336, 785
Sharma S., Bland-Hawthorn J., Johnston K. V., Binney J., 2011, ApJ, 730, 3
Sharma S. et al., 2018, MNRAS, 473, 2004
Skrutskie M. F. et al., 2006, AJ, 131, 1163
Snaith O., Haywood M., Matteo P. D., Lehnert M. D., Combes F., Katz D., Gómez A., 2015, A&A, 578, A87
Stassun K. G., Torres G., 2016, ApJ, 831, L6
Steinmetz M. et al., 2006, AJ, 132, 1645
Stello D. et al., 2017, ApJ, 835, 83
Stinson G. S. et al., 2013, MNRAS, 436, 625
Stonkutė E. et al., 2016, MNRAS, 460, 1131
Ting Y.-S., Conroy C., Goodman A., 2015, ApJ, 807, 104
Tsikoudi V., 1979, ApJ, 234, 842
Valenti J. A., Piskunov N., 1996, A&AS, 118, 595
Vera-Ciro C., D'Onghia E., Navarro J., Abadi M., 2014, ApJ, 794, 173
Villalobos Á., Helmi A., 2008, MNRAS, 391, 1806
Wisnioski E. et al., 2015, ApJ, 209, 799
Wright E. L. et al., 2010, AJ, 140, 1868
Wyse R. F. G., Gilmore G., 1988, AJ, 95, 1404
Wyse R. F. G., Gilmore G., Norris J. E., Wilkinson M. I., Kleyna J. T., Koch A., Evans N. W., Grebel E. K., 2006, ApJ, 639, L13
Yoachim P., Dalcanton J. J., 2006, AJ, 131, 226
Yoshii Y., 1982, PASJ, 34, 365
Zasowski G. et al., 2013, AJ, 146, 81
Zwitter T. et al., 2010, A&A, 522, A54

SUPPORTING INFORMATION

Supplementary data are available at *MNRAS* online.

Table A1: An example of the contents included in the online data table.

Please note: Oxford University Press is not responsible for the content or functionality of any supporting materials supplied by the authors. Any queries (other than missing material) should be directed to the corresponding author for the article.

APPENDIX A: ONLINE DATA TABLE

We have included a data table listing the stars analysed in this work, their GALAH object ID, UCAC4 catalogue ID, coordinates, thick disc membership probability and distances. Table A1 shows an example of the contents included in the online material.

Table A1. An example of the contents included in the online data table. The complete table is available on the publisher website.

GALAH OBJECT ID	UCAC4 ID	RAJ2000 (°)	DEJ2000 (°)	Distance (pc)	Pr(thick)
131216002101010	156-011705	115.5245	−58.9095	1102.72	0.1583
131216002101012	156-011845	116.1019	−58.9680	1502.33	0.0009
131216002101013	156-011859	116.1602	−58.9823	3058.82	0.0188
131216002101018	156-011814	115.9660	−58.9922	854.35	0.0083
131216002101021	155-011860	116.3630	−59.0953	2287.51	0.0180
131216002101023	155-011759	116.0724	−59.0578	2200.28	0.0096
131216002101025	155-011806	116.2236	−59.1011	2078.00	0.2680
131216002101028	156-011737	115.6524	−58.9935	628.69	0.0003
131216002101029	155-011714	115.9342	−59.0706	1578.78	0.0079
131216002101033	155-011844	116.3374	−59.1984	871.58	0.0021

This paper has been typeset from a TEX/LATEX file prepared by the author.